

# DRAFT

## CMS Paper

*The content of this note is intended for CMS internal use and distribution only*

2016/05/20

Head Id: 340136

Archive Id: Unversioned directory

Archive Date: 2016/04/26

Archive Tag: trunk

Search for dark matter in pp collisions at  $\sqrt{s} = 8$  TeV in events with one or more jets including those from hadronically decaying vector bosons and a large missing transverse energy.

The CMS Collaboration

### Abstract

A search is presented for an excess of events with large missing transverse energy in association with at least one highly energetic jet in a data sample of proton-proton interactions at a centre-of-mass energy of 8 TeV. The data correspond to an integrated luminosity of  $19.7 \text{ fb}^{-1}$  collected by the CMS experiment at the LHC. The results are interpreted using a set of simplified models for the production of dark matter via a scalar, pseudoscalar, vector, or axial vector mediator. Additional sensitivity is achieved by tagging events consistent with the jet originating from a hadronically decaying vector boson. No significant excess with respect to the expectation from the standard model is observed and limits on the parameter space of the simplified models are placed.

This box is only visible in draft mode. Please make sure the values below make sense.

PDFAuthor: CMS Collaboration

PDFTitle: Search for dark matter in pp collisions at  $\sqrt{s}=8$  TeV in events with one or more jets including those from hadronically decaying vector bosons and a large missing energy.

PDFSubject: CMS

PDFKeywords: CMS, physics, software, computing

Please also verify that the abstract does not use any user defined symbols



# 1 Introduction

This paper describes a search for dark matter (DM) in events containing an energetic jet and an imbalance in transverse energy ( $E_T^{\text{miss}}$ ) in proton-proton (pp) collisions at a centre-of-mass energy of 8 TeV. The data correspond to an integrated luminosity of  $19.7 \text{ fb}^{-1}$  collected using the Compact Muon Solenoid (CMS) experiment at the CERN Large Hadron Collider (LHC).

The existence of DM is one of the most compelling sources of evidence for physics beyond the standard model (SM) of particle physics, with astrophysical observations suggesting an abundance of a nonbaryonic form of matter in the universe. In theories that extend the SM, production of DM particles is expected at the LHC. Monojet searches [1–6] provide sensitivity to a wide range of models for DM production at the LHC, while mono-V (where  $V=W$  or  $Z$  boson) searches [7–10] target models with associated production of DM with SM vector bosons. While the mono-V searches target more specific models, they benefit from smaller contributions from SM backgrounds. The interpretation of results from these and other DM searches at the LHC have typically used effective field theories that assume heavy mediators and DM production via contact interactions [11]. The results of this analysis are interpreted in the context of a spin-0 or spin-1 mediator decaying to DM pairs using a set of simplified DM models [12–14], that span a broad range of mediator and DM particle properties [15]. This allows for a comparison in sensitivity with respect to direct detection (DD) experiments and retains validity as a description of DM production across the entire kinematic region accessible at the LHC.

This is the first search at CMS to target the hadronic decay modes of the vector bosons in the mono-V channels. The mono-V search uses recently developed techniques designed to exploit information available in the jet’s substructure when the V-boson is highly Lorentz-boosted and uses a multivariate V-tagging technique to identify the individual jets from moderately boosted V-bosons. The events are categorised according to the nature of the jets in the event. The signal extraction is performed by considering the  $E_T^{\text{miss}}$  distribution in each event category, and using additional data control regions to constrain the dominant backgrounds yielding improvements of roughly 60% and 40% respectively in exclusion limits in comparison with the previous CMS monojet analysis [1], using the same dataset.

This paper is structured as follows: Section 2 provides a description of the CMS detector; Section 3 outlines the DM models explored as signal hypotheses; Section 4 provides a description of object reconstruction, event selection and categorisation used in the search; Section 5 describes the modelling of backgrounds used in the signal extraction; Section 6 presents the results and interpretations in the context of simplified models for DM production.

## 2 CMS detector

The CMS detector, described in Ref. [16], is a multi-purpose apparatus designed to study production processes at high-transverse momentum ( $p_T$ ) proton-proton and heavy-ion collisions. A superconducting solenoid occupies its central region, providing a magnetic field of 3.8 T parallel to the beam direction. Charged-particle trajectories are measured by the silicon pixel and strip trackers, which cover a pseudorapidity region of  $|\eta| < 2.5$ . A lead tungstate crystal electromagnetic calorimeter (ECAL) and a brass and scintillator hadron calorimeter (HCAL) surround the tracking volume and cover  $|\eta| < 3$ . The steel and quartz-fiber Cherenkov forward (HF) calorimeter extends the coverage to  $|\eta| < 5$ . A muon system consists of gas-ionisation detectors embedded in the steel flux-return yoke outside the solenoid, that covers  $|\eta| < 2.4$ . The first level of the CMS trigger system, composed of specialised hardware processors, is designed to select the most interesting events in less than  $4 \mu\text{s}$ , using information from the calorimeters

and muon detectors. The high-level trigger processor farm is used to reduce the event rate to a few hundred Hz.

### 3 Signal hypotheses

The signal hypotheses in this search are a set of simplified mediator models [12–14]. These assume the existence of an additional particle, a fermionic dark matter candidate, and an additional interaction that forces the production of DM. In particular, it is assumed that this additional interaction is mediated by a generic spin-0 or spin-1 particle. The interactions are characterised by four distinct Lagrangians, written for a Dirac-fermion DM particle  $\chi$  with mass  $m_{\text{DM}}$  and mediator (S, P, Z', A) with mass  $m_{\text{MED}}$  as,

$$\mathcal{L}_{\text{scalar}} \supset -\frac{1}{2}m_{\text{MED}}^2 S^2 - g_{\text{DM}} S \bar{\chi} \chi - g_q \sum_{q=b,t} \frac{m_q}{v} S \bar{q} q - m_{\text{DM}} \bar{\chi} \chi, \quad (1)$$

$$\mathcal{L}_{\text{pseudoscalar}} \supset -\frac{1}{2}m_{\text{MED}}^2 P^2 - i g_{\text{DM}} P \bar{\chi} \gamma^5 \chi - i g_q \sum_{q=b,t} \frac{m_q}{v} P \bar{q} \gamma^5 q - m_{\text{DM}} \bar{\chi} \chi, \quad (2)$$

$$\mathcal{L}_{\text{vector}} \supset \frac{1}{2}m_{\text{MED}}^2 Z'_\mu Z'^\mu - g_{\text{DM}} Z'_\mu \bar{\chi} \gamma^\mu \chi - g_{\text{SM}} \sum_q Z'_\mu \bar{q} \gamma^\mu q - m_{\text{DM}} \bar{\chi} \chi, \quad (3)$$

$$\mathcal{L}_{\text{axialvector}} \supset \frac{1}{2}m_{\text{MED}}^2 A_\mu A^\mu - g_{\text{DM}} A_\mu \bar{\chi} \gamma^\mu \gamma^5 \chi - g_{\text{SM}} \sum_q A_\mu \bar{q} \gamma^\mu \gamma^5 q - m_{\text{DM}} \bar{\chi} \chi, \quad (4)$$

assuming scalar (S), pseudoscalar (P), vector (Z'), or axial vector (A) mediated interactions and  $v = 246 \text{ GeV}$  is the Higgs potential vacuum expectation value. For the vector and axial vector mediators, the terms  $g_{\text{DM}}$  and  $g_{\text{SM}}$  denote the couplings of the mediator to the DM particle and to SM particles, respectively [17]. In all models considered, these couplings are assumed to be unity ( $g_{\text{SM}} = g_{\text{DM}} = 1$ ). For the scalar and pseudoscalar models,  $g_q = 1$  is assumed for all quark flavours. This implies a Yukawa coupling of the mediator to the SM fermions. The split in terms of axial vector and vector mediators in the Lagrangian is to parallel the existing separation with DD, into spin-dependent (SD) and spin-independent (SI) interactions. Spin-independent can refer to either vector or scalar mediated interactions, between which DD makes no distinction, while spin-dependent interactions refer to axial vector mediated processes.

Pseudoscalar DM-nucleon interaction cross sections are suppressed at non-relativistic DM velocities, which limits the sensitivity from DD experiments [18, 19]. An extension to the scalar and pseudoscalar can be performed by allowing the scalar and pseudoscalar interactions to undergo electroweak symmetry breaking in an analogous way to the Higgs mechanism [20–26]. In collider experiments, the production of Dark Matter in spin-0 mediated interactions is predominantly through gluon-fusion via a top-quark loop (as shown in Fig. 1(a)). When couplings of the mediator to vector bosons are present, mono-V signatures are produced through a radiative process (of Fig. 1(b)). The scenario in which couplings between the mediator and vector bosons are not considered, is denoted herein as *fermionic*. For the spin-1 signatures, DM is produced in an analogous way to Z boson production (as in Figs. 1(c) and (d)). The mono-V and monojet signatures follow from initial-state radiation (ISR) of a V-boson and quark or gluon, respectively. For the fermionic models, the width is determined under the minimum width constraint requiring that only quarks and DM particles couple to the mediator. For the case in which couplings between the mediator and V-bosons are allowed, the width is modified to account for the additional contributions that arise [17].

80 In order to model the contributions expected from these signals, simulated events are gener-  
 81 ated using MCFM6.8[27] for the monojet final state, and JHUGEN5.2.5 [28] for the V-boson  
 82 signature. All signal models are generated at leading order (LO), using PYTHIA6.4.26 [29] for  
 83 parton showers and hadronisation, and GEANT4 [30] for simulation of the CMS detector re-  
 84 sponse. For the monojet signal, the generation is performed using the mediator mass for the  
 85 renormalisation and factorisation scales used to generate the events. The mediator mass is also  
 86 used for the scale in the parton showering (PS). An alternative choice taking the boson  $p_T$  for  
 87 the PS scale is found to result in reductions of 30 – 80% in the expected signal yield in the  
 88 relevant kinematic region for mediator masses above 400 GeV. For scalar and pseudoscalar  
 89 mediated DM production, the finite top quark mass is taken into account for both the inclusive  
 90 and differential cross section. NNPDF3.0 is used to specify the parton distribution function  
 91 (PDF) inputs in the signal generation [31].

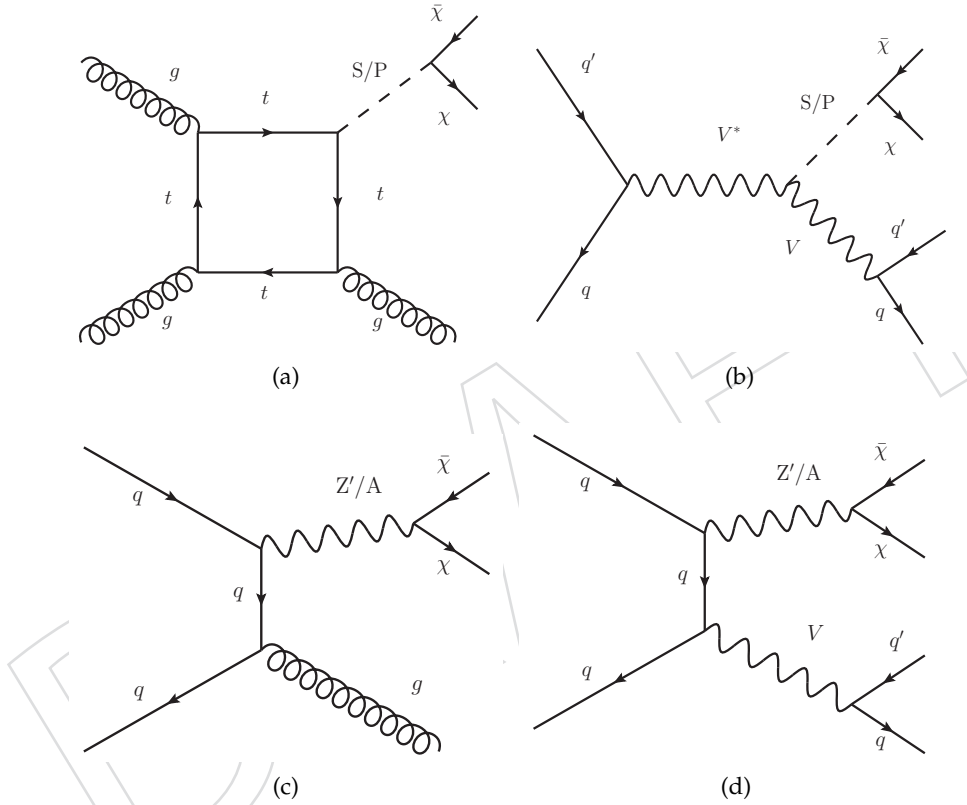


Figure 1: Diagrams for production of DM via mediator (X) in the cases of a scalar/pseudoscalar mediator providing (a) monojet and (b) mono-V signatures. Diagrams for production of DM via a vector/axial vector mediator providing (c) monojet and (d) mono-V signatures.

## 4 Event selection and categorisation

Candidate signal events are selected on the basis of large values of missing transverse energy ( $E_T^{\text{miss}}$ ) and one or more high- $p_T$  jets [16].

The data used for this analysis are collected using two  $E_T^{\text{miss}}$  triggers. The first requires an  $E_T^{\text{miss}}$  of greater than 120 GeV, calculated only using information from the calorimeters, while the second requires  $E_T^{\text{miss}} > 95 \text{ GeV}$  or  $E_T^{\text{miss}} > 105 \text{ GeV}$ , depending on the data taking period, together with at least one jet of  $p_T > 80 \text{ GeV}$  and  $|\eta| < 2.6$ . The  $E_T^{\text{miss}}$  is calculated using the particle flow (PF) reconstruction algorithm [32], which optimally combines information from

various components of the CMS detector to reconstruct and identify individual particles. The lowest threshold on  $E_T^{\text{miss}}$  for event selection is set at 200 GeV to ensure a trigger efficiency greater than 99% for selected events.

Jets are reconstructed by clustering of PF objects using both the anti- $k_T$  algorithm [33] with 0.5 (AK5 jet) as the distance parameter, and the Cambridge–Aachen algorithm [34] with 0.8 distance parameter (CA8). The leading jet is required to pass standard CMS identification criteria [35]. The jets are corrected for contamination from additional, synchronous interactions (pileup, PU) on the basis of the observed event energy density [36]. Further corrections are then applied to calibrate the absolute scale of the jet energy [35].

The  $E_T^{\text{miss}}$  is defined as the magnitude of the vector sum of the  $p_T$  of all final state particles, that are reconstructed using PF. Events with a large mis-reconstructed  $E_T^{\text{miss}}$  are removed by applying a quality filter on the tracker, ECAL, HCAL and muon detector data.

The azimuthal angle  $\phi$  between the  $E_T^{\text{miss}}$  direction and the leading jet in the plane transverse to the beam line,  $\Delta\phi(E_T^{\text{miss}}, j)$ , is required to be larger than 2 radians to reduce the contribution from QCD multijet events. Finally, events are vetoed if they contain at least one well-identified electron, photon or muon with  $p_T > 10$  GeV, or a  $\tau$  lepton with  $p_T > 15$  GeV [37–40]. The electron,  $\tau$  lepton and photon vetoes require that the identified object be isolated using standard PF isolation algorithms [41].

Selected events are classified according to the topology of the jets to distinguish initial or final state radiation from hadronic V-boson decays, which can be either highly Lorentz-boosted or resolved into two jets. This results in three orthogonal categories of events that are referred to as monojet, V-boosted, and V-resolved. The V-boosted and V-resolved categories are collectively referred to as V-tag.

To compute the SM background expectation, simulated samples are produced at LO for the Z+jets, W+jets, tt, single top quark, and QCD multijet processes using MADGRAPH5.1.3 [42] interfaced with, and with PYTHIA6.4.26A for hadronisation and fragmentation, where jets from the matrix element calculations are matched to the parton shower following the MLM matching prescription [43]. Additionally a single top quark background sample, produced at next-to-leading order (NLO) with POWHEG1.0 [44–48], and a set of diboson samples, produced at LO with PYTHIA6.4.26A. All samples are generated using the CT10 PDF set [49]. The MC samples are corrected to account for the distribution of the number of additional pileup interactions observed in the 8 TeV dataset. Both signal and background samples are additionally corrected to account for the mismodeling of hadronic recoil in simulation following the procedure described in Ref. [50].

If the vector boson decays hadronically and has sufficiently large  $p_T$ , both its hadronic decay products are captured as a single reconstructed “fat” jet. Events in the V-boosted category are required to have a reconstructed CA8 jet with  $p_T > 200$  GeV and  $E_T^{\text{miss}} > 250$  GeV. Further selection criteria are applied to improve the vector boson jet purity by cutting on the “N-subjettiness” ratio  $\tau_2/\tau_1$  as defined in Refs. [51, 52], which identifies jets with a two pronged topology, and the pruned jet mass ( $m_{\text{prune}}$ ) [53]. The  $\tau_2/\tau_1$  ratio is required to be smaller than 0.5 and  $m_{\text{prune}}$  is required to be in the range 60–110 GeV. Events which contain additional jets close to the CA8 jet, but no closer than  $\Delta R = \sqrt{\delta\eta^2 + \delta\phi^2} < 0.5$ , are selected to include the frequent cases in which ISR yields additional jets. If an AK5 jet with  $p_T > 30$  GeV and  $|\eta| < 2.5$  is reconstructed, and the azimuthal angle between it and the CA8 jet is smaller than 2 radians, the event is selected, otherwise it is rejected. Events with more than one AK5 jet with  $p_T > 30$  GeV and  $|\eta| < 2.5$ , reconstructed at  $\Delta R > 0.5$  relative to the CA8 jet are rejected. Figure 2



shows the distributions in  $\tau_2/\tau_1$  and  $m_{\text{prune}}$ , before the application of the jet mass selection, in simulation and data for the V-boosted category. A discrepancy is present in the simulation relative to the data, and is attributed to the modelling the parton shower and detector simulation. This disagreement is within the systematic uncertainties of the analysis, a detailed discussion of which can be found in Ref. [54].

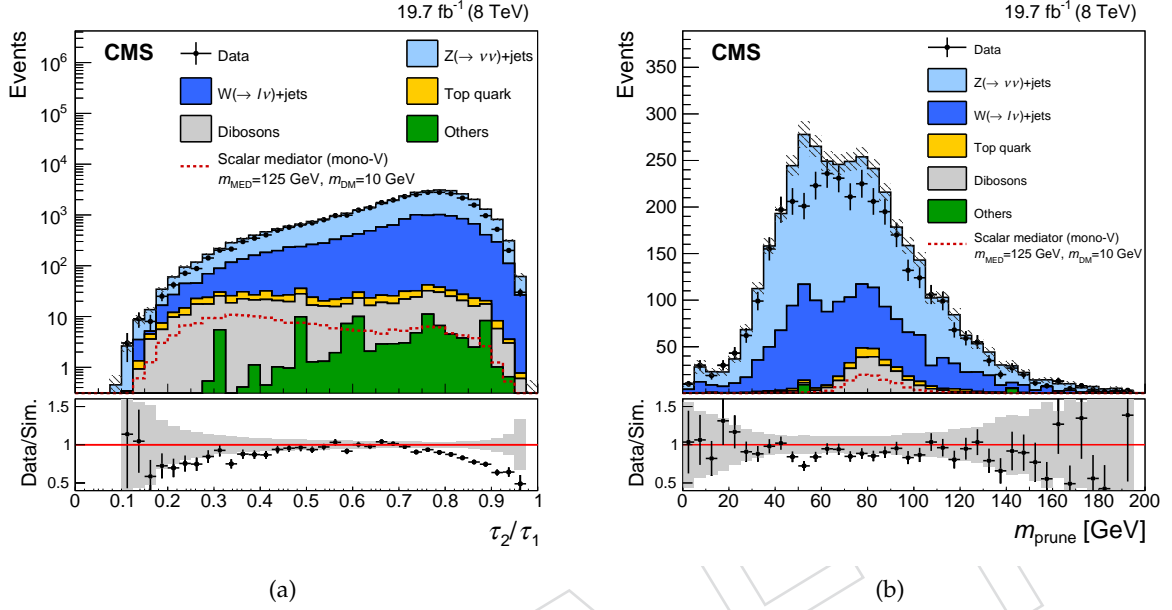


Figure 2: Distributions in highly Lorentz-boosted events before the jet mass selection of (a)  $\tau_2/\tau_1$  and (b)  $m_{\text{prune}}$  for CA8 jets. A requirement of  $\tau_2/\tau_1 < 0.5$  has been applied in (b). The discrepancy between data and simulation is within systematic uncertainties (not shown). The dashed red line shows the expected distribution for scalar-mediated DM production with  $m_{\text{DM}} = 10 \text{ GeV}$  and  $m_{\text{MED}} = 125 \text{ GeV}$ . The gray bands in the bottom panels indicate the statistical uncertainty from the limited number of simulated events.

In cases where the electroweak boson has insufficient boost for its hadronic decay to be fully contained in a single reconstructed fat jet, a selection is applied for decays into a pair of AK5 jets to recover the event if it fails the V-boosted selection. The selection requires that each jet has  $p_T > 30 \text{ GeV}$  and  $|\eta| < 2.5$ , and that the dijet has a mass in the range  $60 - 110 \text{ GeV}$ , consistent with originating from a W or Z boson. To further reduce the combinatorial background in the V-resolved category, a multivariate (MVA) selection criterion is applied. The inputs to the MVA are the likelihood-based discriminators which distinguish quark from gluon jets [55], the jet pull angle [56] and the mass drop variable [57]. In events where multiple dijet pairs are found, the pair with the highest MVA output value is taken as the candidate. The distribution of the MVA output for SM backgrounds and for a scalar mediator produced in association with either a W or Z boson is shown in Fig. 3. Events are selected in the V-resolved category in they have an MVA output greater than 0.6.

To reduce contamination from top quark backgrounds, events are rejected if they contain a b-tagged jet, defined using an MVA discriminator that uses secondary vertex information, and operated at a medium working point (“CSV medium”) [58]. Finally, the events are required to have  $E_T^{\text{miss}} > 250 \text{ GeV}$ .

The events that do not qualify for either of the two V-tagged categories are required to have

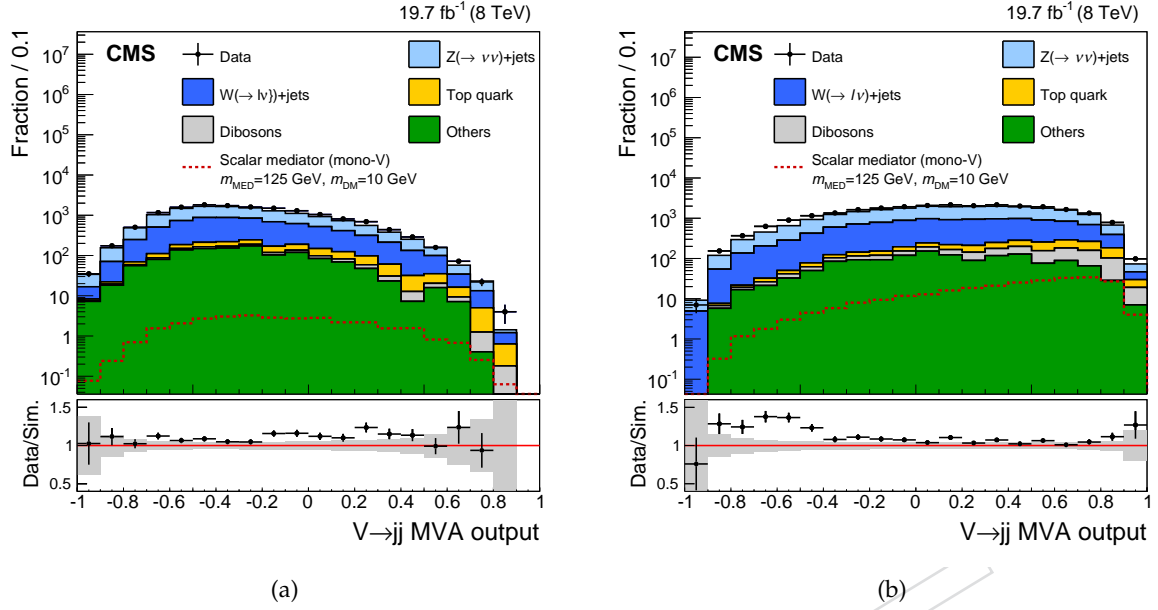


Figure 3: MVA output distribution for V-tag events in simulation and data after signal selection for (a)  $p_T < 160$  GeV and (b)  $p_T > 160$  GeV. At a  $p_T$  of about 160 GeV, the jets begin to overlap. The dashed red line shows the expected distribution for scalar-mediated DM production with  $m_{DM} = 10$  GeV and  $m_{MED} = 125$  GeV. The gray bands in the bottom panels indicate the statistical uncertainty from the limited number of simulated events.

one or two high  $p_T$  jets showing characteristics indicative of originating from a single quark or gluon. This final category is referred to herein as the monojet category. For the monojet category, at least one AK5 jet within  $|\eta| < 2.0$  with  $p_T > 150$  GeV is required and the event must have  $E_T^{miss} > 200$  GeV. As in the V-boosted category, events with a second AK5 jet close to the leading one ( $\Delta\phi(j_1, j_2) < 2$  radians) with  $p_T > 30$  GeV and  $|\eta| < 2.5$  are selected to allow the frequent cases where ISR yields two jets. Events with three or more AK5 jets with  $p_T > 30$  GeV and  $|\eta| < 2.5$  are rejected. Table 1 gives a summary of the event selection in the three categories. The priority for event selection is that events are first selected in the V-boosted, followed by the V-resolved and finally the monojet. Events which pass a given selection are not allowed to enter a subsequent category.

Figure 4 shows the  $E_T^{miss}$  and leading jet  $p_T$  distributions in data and simulation after selection combining the three event classes combined. The backgrounds are normalised to full data integrated luminosity ( $19.7 \text{ fb}^{-1}$ ) and the expected distribution for vector mediated DM production assuming a DM mass of 10 GeV and mediator mass of 1 TeV is shown. The discrepancy between the data and simulation is a result of both detector resolution and an imperfect theoretical description of the kinematics of the V+jets processes, which are corrected using control samples in data described in the following section.



Table 1: Event selections for the V-boosted, V-resolved and monojet categories. The requirements on  $p_T^j$  and  $|\eta|^j$  refer to the highest  $p_T$  CA8 or AK5 jet in the V-boosted or monojet categories, and to both leading AK5 jets in the V-resolved category.

	V-boosted	V-resolved	Monojet
$p_T^j$	$> 200 \text{ GeV}$	$> 30 \text{ GeV}$	$> 200 \text{ GeV}$
$ \eta ^j$	$< 2.5$	$< 2$	$< 2$
$E_T^{\text{miss}}$	$> 250 \text{ GeV}$	$> 250 \text{ GeV}$	$> 200 \text{ GeV}$
$\tau_2/\tau_1$	$< 0.5$	-	-
V $\rightarrow$ jj MVA output	-	$> 0.6$	-
$m_{\text{prune}}/m_{jj}^\dagger$	$60 - 110 \text{ GeV}$	$60 - 110 \text{ GeV}$	-
$\Delta\phi(E_T^{\text{miss}}, j)$	$> 2 \text{ rad}$	-	$> 2 \text{ rad}$
$N_j^\ddagger$	$= 1$	-	$= 1$

<sup>†</sup> The cut on the mass refers to  $m_{\text{prune}}$  in the V-boosted category and the dijet invariant mass  $m_{jj}$  in the V-resolved category.

<sup>‡</sup> An additional jet is allowed only if it falls within  $\Delta\phi < 2$  radians of the leading AK5 or CA8 jet for the monojet or V-boosted category. The additional AK5 jets in the V-boosted category must be further than  $\Delta R > 0.5$  for the event to fail this criteria.

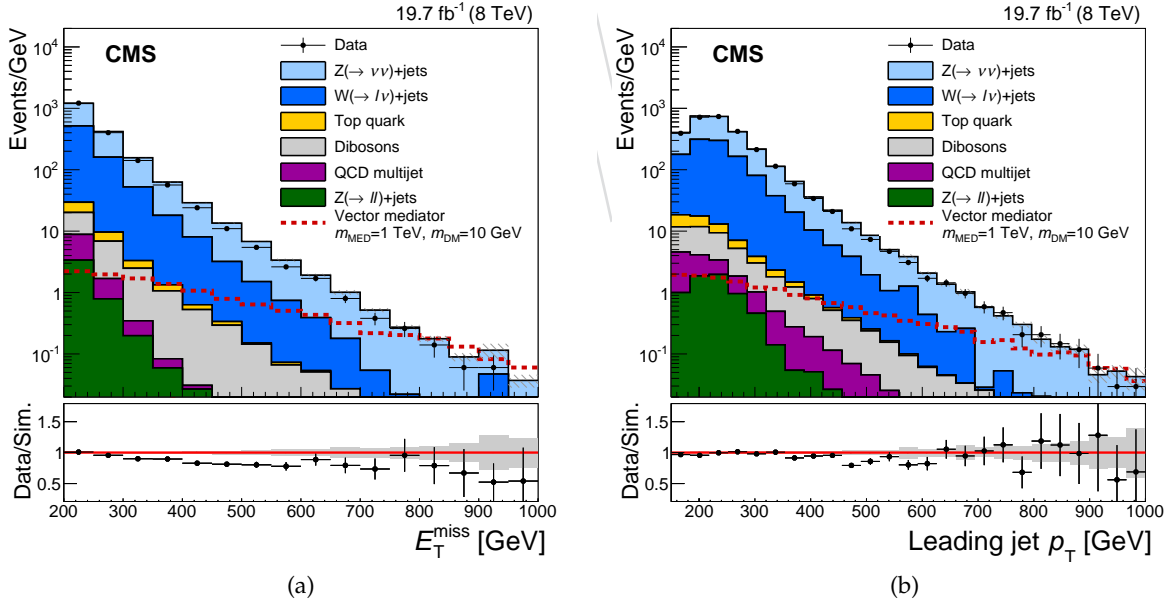


Figure 4: Distributions in (a)  $E_T^{\text{miss}}$  and (b) leading jet  $p_T$  in simulated events and data, combining the signal selections for the three event categories. The dashed red line shows the expected distribution assuming vector mediated DM production with  $m_{\text{DM}} = 10 \text{ GeV}$  and  $m_{\text{MED}} = 1 \text{ TeV}$ . The gray bands in the bottom panels indicate the statistical uncertainty from the limited number of simulated events.

## 5 Background estimation

The presence of DM production will be observable as an excess of events above SM backgrounds at high  $E_T^{\text{miss}}$ . Significant improvements in terms of sensitivity can be expected if several bins in  $E_T^{\text{miss}}$ , yielding the  $E_T^{\text{miss}}$  shape, are considered simultaneously. Further improvement is achieved by using control regions in data to reduce the uncertainties on the predictions of the SM backgrounds. These regions are statistically independent from the signal region and designed such that the expected contribution from a potential signal is negligible. A binned likelihood fit is performed in the ranges 250–1000 GeV and 200–1000 GeV for the V-tag (V-boosted and V-resolved) and monojet events, respectively. The binning is chosen to ensure each corresponding bin of a set of control regions is populated. The width of the highest  $E_T^{\text{miss}}$  bin is chosen to provide ease of comparison to the previous CMS search [1].

The background contributions from  $Z(\nu\nu)$ +jets ( $W(l\nu)$ +jets) is determined using data from dimuon and photon (single muon) control regions. The dimuon control region is defined using the same selection as for the signal region, but removing the muon veto. Instead, exactly two isolated muons are required with opposite charge,  $p_T^{\mu_1}, p_T^{\mu_2} > 20, 10$  GeV and an invariant mass in the range 60 – 120 GeV.

As the decay branching ratio of  $Z \rightarrow \mu^+ \mu^-$  is approximately six times smaller than that to neutrinos, the resulting statistical uncertainty in the  $Z(\nu\nu)$ +jets background becomes a dominant systematic uncertainty at large values of  $E_T^{\text{miss}}$ . A complementary approach is to use events in data that have a high- $p_T$  photon recoiling against jets to further constrain the  $Z(\nu\nu)$ +jets. This is advantageous since the production cross section of  $\gamma$ +jets is roughly a factor of three times that of the  $Z(\nu\nu)$ +jets, yielding thereby a smaller statistical uncertainty in the predicted background. The theoretical uncertainties associated to the translation of the kinematics in  $\gamma$ +jets events to that of  $Z(\nu\nu)$ +jets events are however significant. A combination of both photon and dimuon control regions is therefore used to maximally constrain the  $Z(\nu\nu)$ +jets background.

The photon control region consists of events which are selected by a trigger requiring an isolated photon with  $p_T > 150$  GeV [37]. The selected events are required to have at least one photon with  $p_T > 170$  GeV and  $|\eta| < 2.5$ , identified using a medium efficiency selection criteria [37]. Photons in the ECAL transition region,  $1.44 < |\eta| < 1.56$  are excluded. All other kinematic selections are the same as the signal region, except for the  $E_T^{\text{miss}}$ . The purity of the selection has been measured and is used to estimate the contributions from other backgrounds in the photon control region [37].

To estimate the  $W(l\nu)$ +jets background, a single muon control region is defined by selecting events with exactly one muon with  $p_T > 20$  GeV. Additionally the transverse mass, calculated as  $m_T = \sqrt{2E_T^{\text{miss}}p_T^\mu(1 - \cos\phi)}$ , where  $\phi$  is the azimuthal angle between the muon and  $E_T^{\text{miss}}$  vector, is required to be in the range 50 – 100 GeV.

The events in the control regions are divided into the three categories, using the same selection criteria described in Section 4, but in addition requiring the presence of a pair of oppositely charged muons consistent with a Z boson decay, a high  $p_T$  photon or a single muon consistent with being a leptonic W boson decay. This yields a total of nine control regions; three for each event category. In the control regions, the momentum of the dimuon pair, single muon or the photon is removed and the  $E_T^{\text{miss}}$  is recalculated. This quantity is referred to as pseudo- $E_T^{\text{miss}}$  and it is this variable to which the  $E_T^{\text{miss}}$  selection of the corresponding signal region applies. The distribution of pseudo- $E_T^{\text{miss}}$  in the control regions is used to estimate the distribution of  $E_T$  expected from the  $Z(\nu\nu)$ +jets and  $W(l\nu)$ +jets backgrounds in the signal region.

The  $E_T^{\text{miss}}$  spectra of the backgrounds are determined through the use of the binned likelihood fit, to the data in all the bins of the three control regions. The expected number of events  $N_i$  in a given bin  $i$  of pseudo- $E_T^{\text{miss}}$ , is defined as  $N_i^{Z\mu\mu} = \mu_i^{Z\rightarrow\nu\nu}/R^Z$  and  $N_i^\gamma = \mu_i^{Z\rightarrow\nu\nu}/R^\gamma$  for the dimuon and photon control regions and  $N_i^W = \mu_i^{W\nu}/R_i^W$ , for the single muon control region. The  $\mu_i^{Z\rightarrow\nu\nu}$  and  $\mu_i^{W\nu}$  terms are free parameters of the likelihood representing the yields of  $Z(\nu\nu)$ +jets and  $W(l\nu)$ +jets in each bin of the signal region. The additional terms  $R_i^W$ ,  $R_i^{Z|\gamma}$  denote factors that account for the extrapolation of specific backgrounds from the signal region to control regions. The likelihood function for a particular category is given by

$$\begin{aligned} \mathcal{L}(\mu^{Z\rightarrow\nu\nu}, \mu^{W\nu}, \alpha, \beta) = & \prod_i \text{Poisson} \left( d_i^\gamma | B_i^\gamma(\alpha) + \frac{\mu_i^{Z\rightarrow\nu\nu}}{R_i^\gamma(\beta)} \right) \\ & \times \prod_i \text{Poisson} \left( d_i^Z | B_i^Z(\alpha) + \frac{\mu_i^{Z\rightarrow\nu\nu}}{R_i^Z(\beta)} \right) \\ & \times \prod_i \text{Poisson} \left( d_i^W | B_i^W(\alpha) + \frac{\mu_i^{W\nu}}{R_i^W(\beta)} \right), \end{aligned} \quad (5)$$

where  $d_i^\gamma$ ,  $d_i^Z$  and  $d_i^W$  are the observed number of events in each bin of the photon, dimuon and single muon control regions. Additionally,  $\alpha, \beta$  denote parameters profiled over during the likelihood minimisation, and Poisson denotes its eponymous distribution. The expected contributions from background processes in the photon, dimuon and single muon control regions are denoted  $B^\gamma$ ,  $B^Z$  and  $B^W$  in Equation (5), respectively.

The factors  $R_i^Z$  account for the ratio of  $B(Z \rightarrow \nu\nu)/B(Z \rightarrow \mu^+\mu^-)$  and the muon efficiency times acceptance in the dimuon control region, while  $R_i^\gamma$  account for the ratio of differential cross section between the  $Z$ +jets and  $\gamma$ +jets processes, and the efficiency times acceptance of the photon selection for the  $\gamma$ +jets control region. The differential cross sections of photon and  $Z$  production are first corrected using NLO K-factors obtained from a comparison of their  $p_T$  distributions in events generated with MADGRAPH5\_AMC@NLOV5.2.2.2 [42], to the distributions produced at LO. These K-factors are used to correct the factors  $R_i^\gamma$  to account for NLO QCD effects.

Systematic uncertainties are modelled as constrained nuisance parameters which allow for variation of the factors  $R^\gamma$ ,  $R^Z$  and  $R^W$  in the fit, and are treated as fully correlated between event categories. These include theoretical uncertainties on the photon to  $Z$  differential cross section ratio from renormalisation and factorisation scale uncertainties which amount to 8% each across the relevant boson  $p_T$  range. These uncertainties are conservative in that they are estimated taking the maximum difference due to the scale variation for an individual process on the ratio thereby ignoring any cancellation of the scale uncertainties. Electroweak corrections are not accounted for in the simulation. Additional K-factors are applied as a function of the boson ( $Z$  or  $\gamma$ )  $p_T$ , to account for higher order electroweak effects which are around 15% for a boson  $p_T$  around 1 TeV [59]. The full correction is taken as an uncertainty in the ratio. A conservative choice is made in assuming this uncertainty to be uncorrelated across bins of  $E_T^{\text{miss}}$ . The uncertainties in the muon selection efficiency, photon selection efficiency, and photon purity are included and fully correlated across the control regions for the three event categories. The results of the fit to the control regions for the V-boosted, V-resolved and monojet categories are shown in Figs. 5, 6, and 7, respectively.

The remaining backgrounds are expected to be much smaller than those from V+jets and are

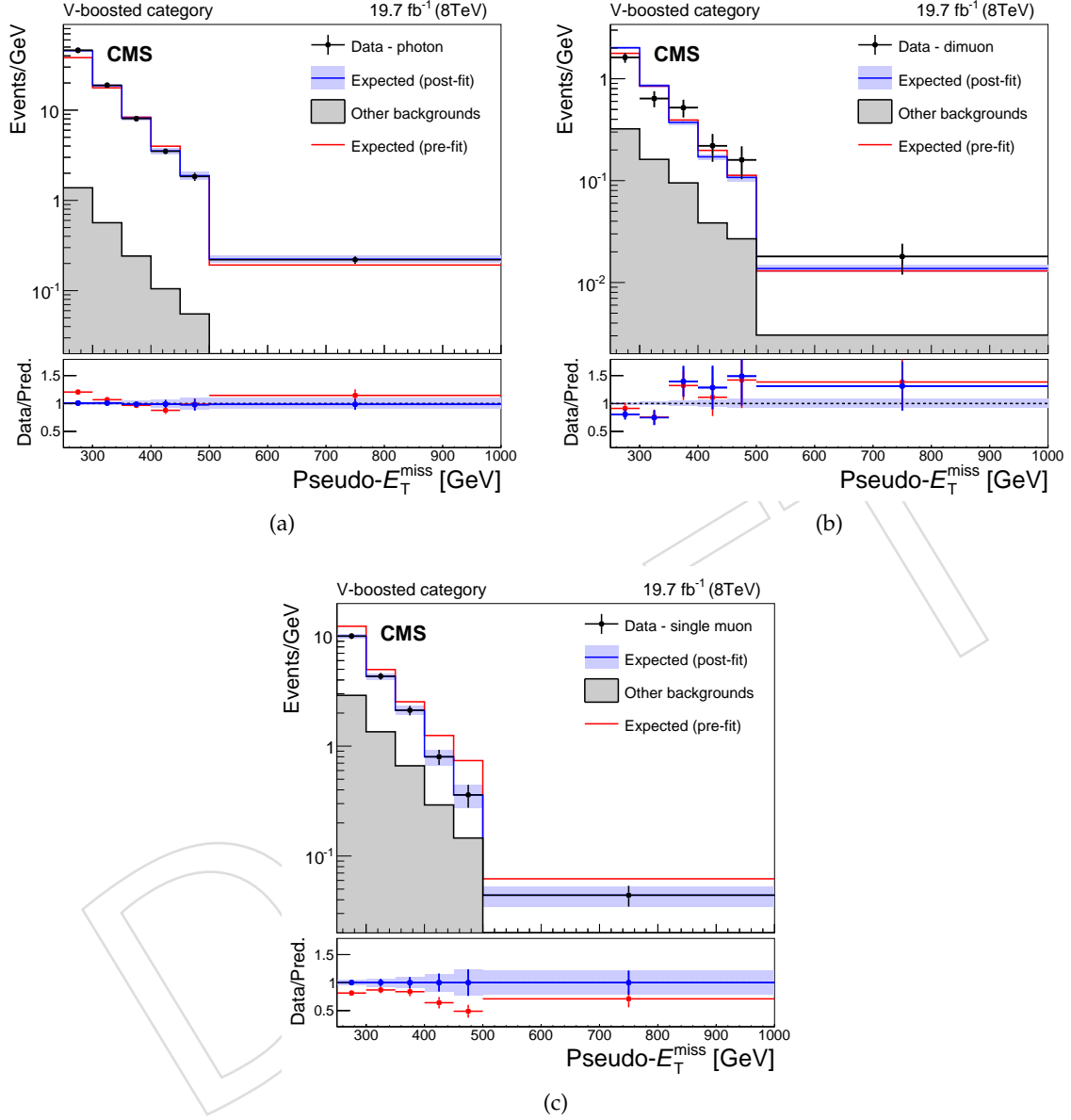


Figure 5: Expected and observed pseudo- $E_T^{\text{miss}}$  distributions in the photon (a), dimuon (b) and single muon (c) control regions, before and after performing the simultaneous likelihood fit to the data in the control regions, for the V-booster category. The red line represents the expected distribution before fitting the control regions, while the blue line shows the expectation after the fit. The bottom panels show the ratio of the observed data to the expectations before (pre) and after (post) the fit. The blue bands indicate the combined statistical and systematic uncertainties from the fit.

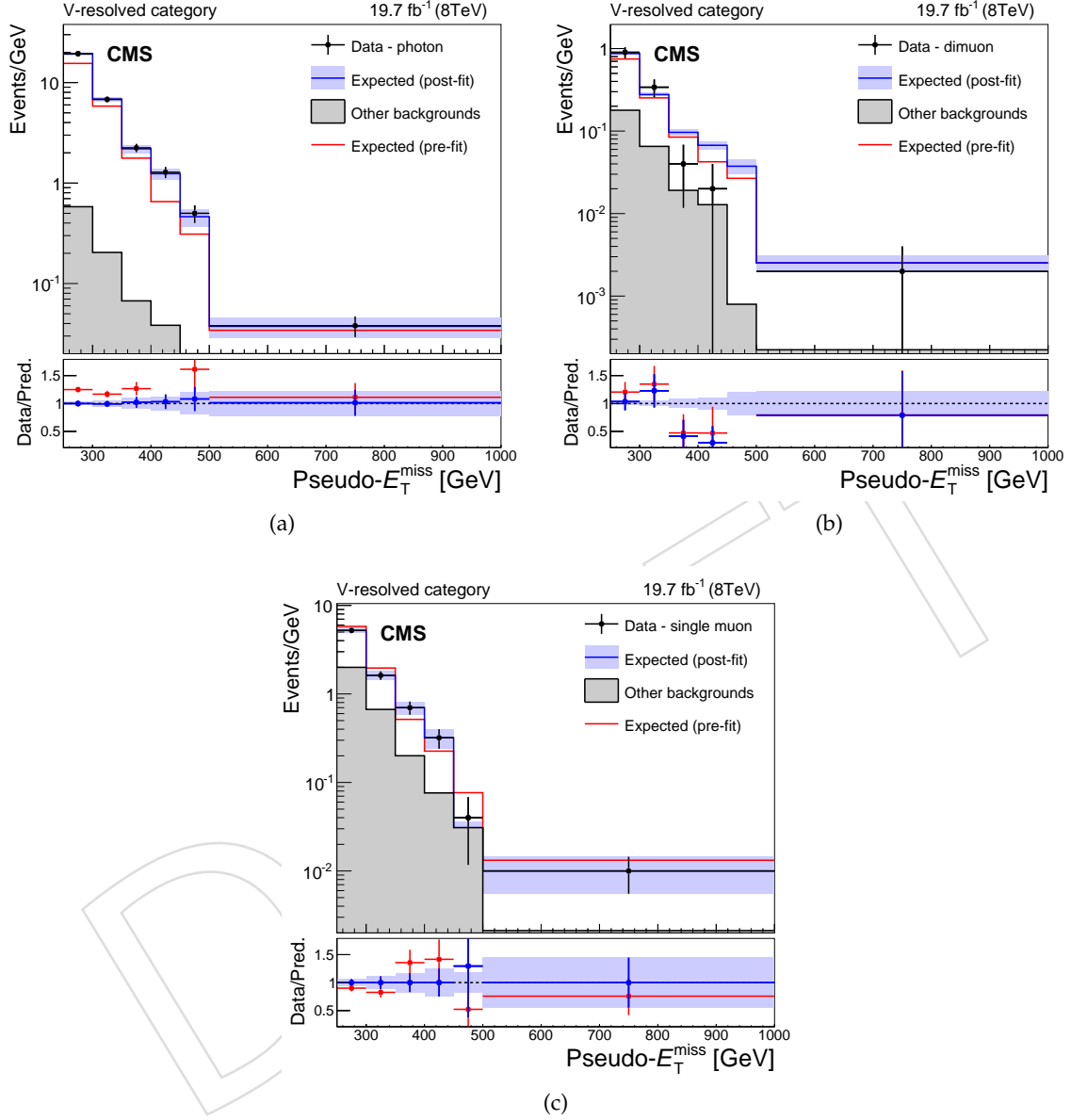


Figure 6: Expected and observed pseudo- $E_T^{\text{miss}}$  distributions in the photon (a), dimuon (b) and single muon (c) control regions, before and after performing the simultaneous likelihood fit to the data in the control regions, for the V-resolved category. The red line represents the expected distribution before fitting the control regions, while the blue line shows the expectation after the fit. The bottom panels show the ratio of the observed data to the expectations before (pre) and after (post) the fit. The blue bands indicate the combined statistical and systematic uncertainties from the fit.

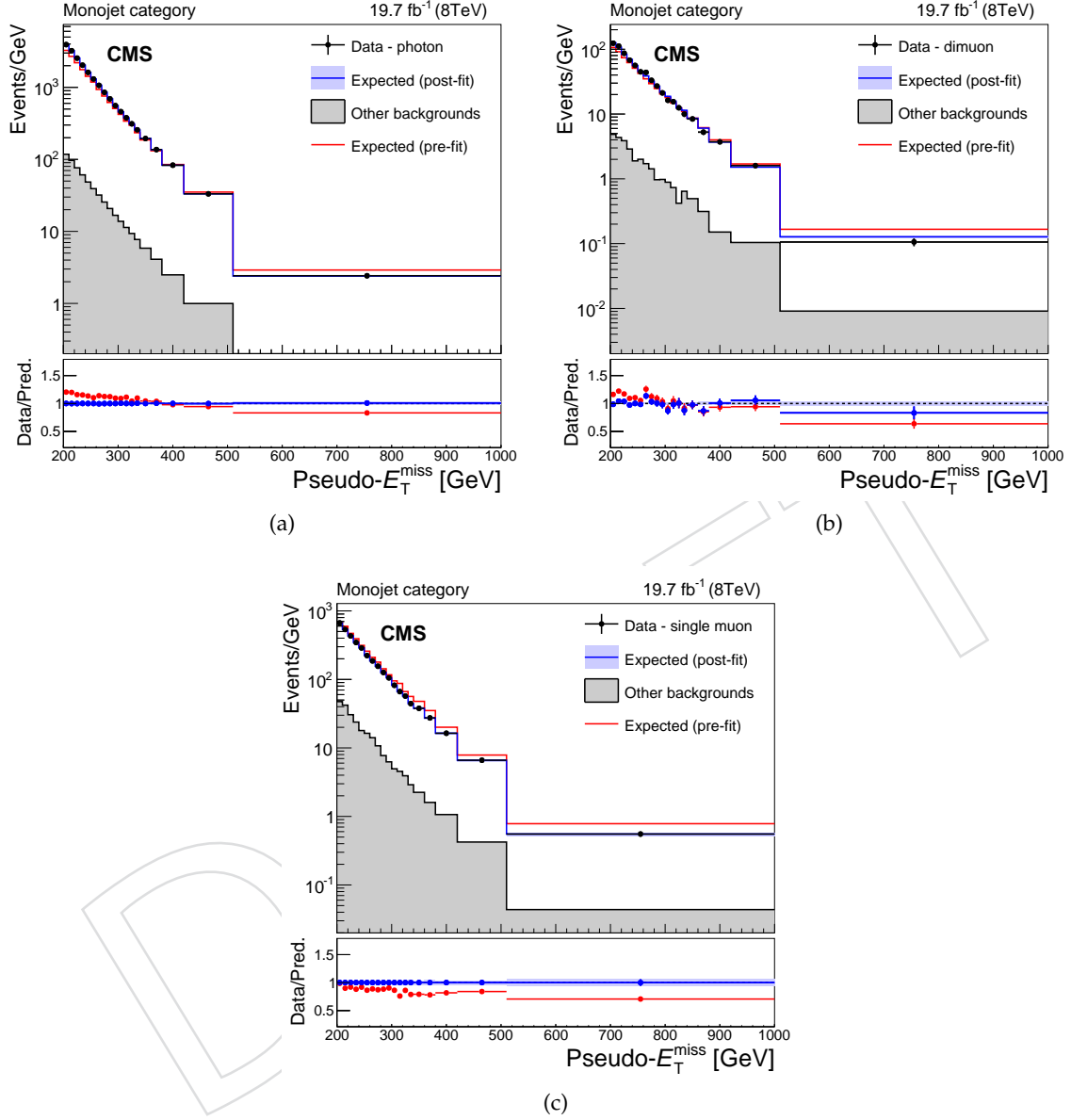


Figure 7: Expected and observed pseudo- $E_T^{\text{miss}}$  distributions in the photon (a), dimuon (b) and single muon (c) control regions before and after performing the simultaneous likelihood fit to the data in the control regions, for the monojet category. The red line represents the expected distribution before fitting the control regions, while the blue line shows the expectation after the fit. The bottom panels show the ratio of the observed data to the expectations before (pre) and after (post) the fit. The blue bands indicate the combined statistical and systematic uncertainties from the fit.



estimated directly from the simulation. Shape and normalisation systematic uncertainties from the recoil corrections applied to these backgrounds are included to account for the uncertainty in the jet energy scale and resolution. In addition, a systematic uncertainty of 4% is included for the top quark backgrounds due to the uncertainty of the b-tagging efficiency for the b-jet veto in the V-resolved category [60]. Systematic uncertainties of 7% and 10% are included on the normalisations of the top [61] and diboson [62, 63] backgrounds, respectively to account for the uncertainty in their cross sections in the relevant kinematic phase-space. These individual backgrounds have been studied separately using dedicated control regions in data to validate these systematic uncertainties. A systematic uncertainty of 50% is included on the expected contribution from QCD multijet events. This uncertainty was obtained by taking the largest differences observed between data and simulation in events selected by inverting the requirement on  $\Delta(E_T^{\text{miss}}, j)$ . Finally, a systematic uncertainty of 2.6% in the luminosity measurement [64] is included for all of the backgrounds obtained from simulation.

The expected yields in each bin of  $E_T^{\text{miss}}$  from all SM backgrounds, after the fit in the control regions, for each of the three signal regions, are given in Tables 2, 3 and 4. The uncertainties represent the sum in quadrature of the effects of all the relevant sources of systematic uncertainty in each bin of  $E_T^{\text{miss}}$ . The potential correlations of the uncertainties between the different  $E_T^{\text{miss}}$  bins are not reflected in these numbers.

Table 2: Expected yields of the SM processes and their uncertainties per bin for the monojet category after the fit to the control regions.

$E_T^{\text{miss}}$ (GeV)	Obs.	Z( $\rightarrow \nu\nu$ )+jets	W( $\rightarrow l\nu$ )+jets	Top quark	Dibosons	Other	Total Bkg.
200 - 210	17547	10740 $\pm$ 270	6770 $\pm$ 320	132 $\pm$ 11	135 $\pm$ 14	540 $\pm$ 220	18330 $\pm$ 600
210 - 220	14303	9230 $\pm$ 230	4990 $\pm$ 240	104 $\pm$ 13	112 $\pm$ 11	58.0 $\pm$ 4.3	14500 $\pm$ 610
220 - 230	11343	7320 $\pm$ 190	3830 $\pm$ 170	82.1 $\pm$ 7.3	95.1 $\pm$ 9.6	44.8 $\pm$ 3.6	11370 $\pm$ 400
230 - 240	8961	5730 $\pm$ 170	3020 $\pm$ 160	62.0 $\pm$ 5.8	77.9 $\pm$ 8.6	111 $\pm$ 19	8940 $\pm$ 400
240 - 250	6920	4680 $\pm$ 150	2470 $\pm$ 140	46.6 $\pm$ 4.4	61.0 $\pm$ 6.1	79 $\pm$ 12	7290 $\pm$ 330
250 - 260	5582	3700 $\pm$ 140	1860 $\pm$ 120	34.2 $\pm$ 3.7	50.1 $\pm$ 4.9	48.1 $\pm$ 6.3	5670 $\pm$ 370
260 - 270	4517	3290 $\pm$ 130	1580 $\pm$ 110	27.7 $\pm$ 2.3	39.7 $\pm$ 4.2	11.9 $\pm$ 0.4	4950 $\pm$ 320
270 - 280	3693	2570 $\pm$ 110	1101 $\pm$ 71	25.0 $\pm$ 3.1	33.5 $\pm$ 3.4	23.3 $\pm$ 2.7	3740 $\pm$ 160
280 - 290	2907	2085 $\pm$ 89	934 $\pm$ 71	17.8 $\pm$ 1.9	28.1 $\pm$ 3.0	5.4 $\pm$ 0.1	3070 $\pm$ 180
290 - 300	2406	1721 $\pm$ 85	754 $\pm$ 58	15.0 $\pm$ 3.6	21.9 $\pm$ 2.7	80.7 $\pm$ 11	2530 $\pm$ 170
300 - 310	1902	1337 $\pm$ 79	577 $\pm$ 51	8.9 $\pm$ 1.6	17.7 $\pm$ 2.1	3.1 $\pm$ 0.1	1950 $\pm$ 160
310 - 320	1523	1182 $\pm$ 58	435 $\pm$ 43	5.9 $\pm$ 2.2	15.5 $\pm$ 1.8	81 $\pm$ 10	1650 $\pm$ 110
320 - 330	1316	931 $\pm$ 53	371 $\pm$ 44	5.2 $\pm$ 1.3	11.0 $\pm$ 1.8	2.1 $\pm$ 0.1	1321 $\pm$ 92
330 - 340	1065	804 $\pm$ 51	246 $\pm$ 29	4.9 $\pm$ 1.1	11.9 $\pm$ 1.8	1.8 $\pm$ 0.1	1070 $\pm$ 120
340 - 360	1571	1225 $\pm$ 61	399 $\pm$ 39	6.8 $\pm$ 1.2	16.4 $\pm$ 1.6	5.6 $\pm$ 0.4	1650 $\pm$ 110
360 - 380	1091	822 $\pm$ 53	269 $\pm$ 30	3.4 $\pm$ 0.4	13.3 $\pm$ 1.4	1.3 $\pm$ 0.1	1110 $\pm$ 150
380 - 420	1404	1036 $\pm$ 66	324 $\pm$ 30	5.5 $\pm$ 0.6	17.1 $\pm$ 1.7	1.4 $\pm$ 0.1	1390 $\pm$ 110
420 - 510	1126	943 $\pm$ 70	267 $\pm$ 27	3.9 $\pm$ 0.8	15.7 $\pm$ 1.6	92.7 $\pm$ 9.7	1240 $\pm$ 140
510 - 1000	476	330 $\pm$ 32	72 $\pm$ 12	0.6 $\pm$ 0.2	8.2 $\pm$ 0.8	0.3 $\pm$ 0.1	410 $\pm$ 71

## 6 Results

A simultaneous fit is performed to the signal region across the three event categories, allowing for systematic uncertainties in the background expectations. The corresponding comparisons between data and background in the  $E_T^{\text{miss}}$  distributions, for each of the three categories, after this fit are shown in Fig. 8. Agreement between the expected SM backgrounds and data is observed at the percent level across the three categories. A local significance of the data in each bin is calculated by comparing the likelihood between the background-only fit (Fig. 8) and another fit, setting the expected total yield of events in that bin to the observation in data. The largest local significance observed using this procedure is 1.9 standard deviations and corresponds to the largest  $E_T^{\text{miss}}$  bin of the monojet category.

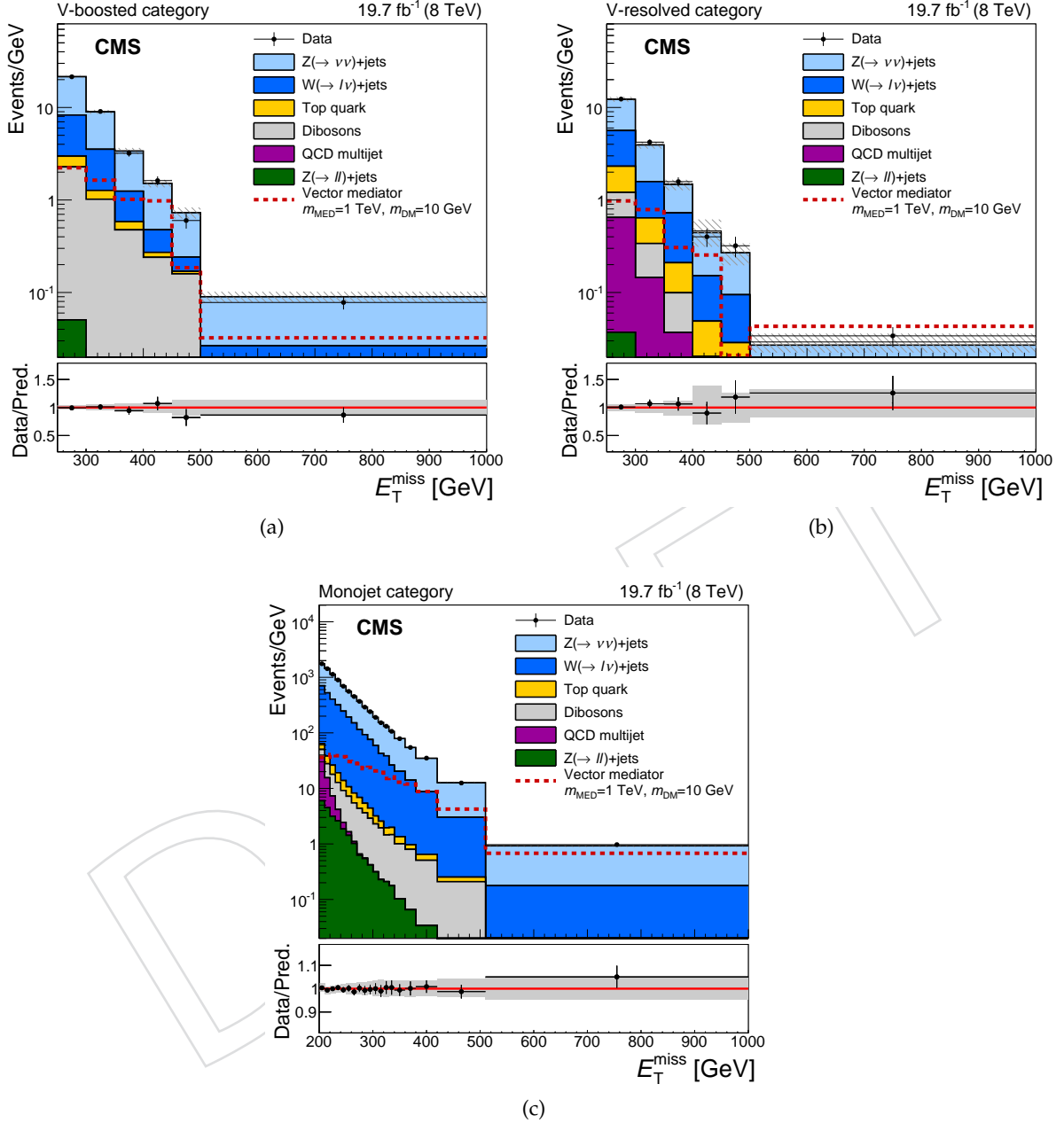


Figure 8: Post-fit distributions in  $E_T^{\text{miss}}$  expected from SM backgrounds and observed in the signal region. The expected distributions are evaluated after fitting to the observed data simultaneously across the (a) V-booster, (b) V-resolved and (c) monojet categories. The gray bands indicate the post-fit uncertainty in the background, assuming no signal. The expected distribution assuming vector mediated DM production is shown for  $m_{\text{DM}} = 10$  GeV and  $m_{\text{MED}} = 1$  TeV.

Table 3: Expected yields of the SM processes and their uncertainties per bin for the V-resolved category after the fit to the control regions.

$E_T^{\text{miss}}$ (GeV)	Obs.	Z( $\rightarrow \nu\nu$ )+jets	W( $\rightarrow l\nu$ )+jets	Top quark	Dibosons	Other	Total Bkg.
250 - 300	617	298 $\pm$ 36	166 $\pm$ 26	55.4 $\pm$ 4.7	27.9 $\pm$ 1.6	39 $\pm$ 17	587 $\pm$ 48
300 - 350	211	98 $\pm$ 14	41 $\pm$ 10	15.2 $\pm$ 1.5	9.6 $\pm$ 0.3	12.3 $\pm$ 3.8	170 $\pm$ 18
350 - 400	79	31.1 $\pm$ 7.0	21.5 $\pm$ 8.9	5.5 $\pm$ 0.7	3.2 $\pm$ 0.3	2.0 $\pm$ 0.4	62 $\pm$ 12
400 - 450	20	20.1 $\pm$ 6.4	14.5 $\pm$ 8.5	1.5 $\pm$ 0.2	0.6 $\pm$ 0.3	6.3 $\pm$ 1.4	38 $\pm$ 11
450 - 500	16	6.1 $\pm$ 2.7	1.0 $\pm$ 2.6	1.0 $\pm$ 0.4	0.4 $\pm$ 0.1	< 1.4	8.5 $\pm$ 3.6
500 - 1000	17	6.9 $\pm$ 3.0	2.6 $\pm$ 1.7	0.3 $\pm$ 0.2	0.5 $\pm$ 0.0	7.6 $\pm$ 1.4	11.6 $\pm$ 3.5

Table 4: Expected yields of the SM processes and their uncertainties per bin for the V-boosted category after the fit to the control regions.

$E_T^{\text{miss}}$ (GeV)	Obs.	Z( $\rightarrow \nu\nu$ )+jets	W( $\rightarrow l\nu$ )+jets	Top quark	Dibosons	Other	Total Bkg.
250 - 300	1073	683 $\pm$ 40	279 $\pm$ 33	35.4 $\pm$ 3.7	103 $\pm$ 15	2.5 $\pm$ 0.1	1103 $\pm$ 63
300 - 350	453	271 $\pm$ 23	114 $\pm$ 20	12.7 $\pm$ 1.3	46.5 $\pm$ 6.9	0.7 $\pm$ 0.1	446 $\pm$ 34
350 - 400	160	118 $\pm$ 13	38.3 $\pm$ 8.7	5.6 $\pm$ 1.0	22.2 $\pm$ 3.3	0.2 $\pm$ 0.1	184 $\pm$ 18
400 - 450	81	49.7 $\pm$ 7.3	9.8 $\pm$ 3.4	1.5 $\pm$ 0.8	11.0 $\pm$ 1.8	< 0.1	72 $\pm$ 29
450 - 500	30	31.2 $\pm$ 6.1	5.0 $\pm$ 2.6	0.5 $\pm$ 0.1	7.4 $\pm$ 1.1	< 0.1	44.3 $\pm$ 6.6
500 - 1000	39	39.8 $\pm$ 7.8	6.4 $\pm$ 3.4	0.2 $\pm$ 0.0	7.8 $\pm$ 1.1	< 0.1	54.3 $\pm$ 8.5

Exclusion limits are set for these models using the asymptotic CLs method [65–67] with a profile likelihood ratio as the test statistic in which systematic uncertainties are modelled as nuisance parameters. For each signal hypothesis tested, upper limits are placed on the ratio of the signal yield to that predicted by the simplified model, denoted as  $\mu$ . Limits are presented in terms of excluded regions in the  $m_{\text{MED}} - m_{\text{DM}}$  plane, assuming scalar, pseudoscalar, vector, and axial-vector mediators, and determining the points for which  $\mu > 1$  is excluded at least at the 90% confidence level (CL). The choice of determining 90% CL is to allow for comparison with other experiments. Experimental systematic uncertainties, including jet and  $E_T^{\text{miss}}$  response and resolution, are included in the signal model as nuisance parameters, while the theoretical systematic uncertainties on the inclusive cross section (20% and 30% for the vector and axial vector, and scalar and pseudoscalar models, respectively) due to QCD scale and PDF uncertainties are instead added as additional contours on the exclusion limits. These uncertainties are chosen for the full range of the mediator mass from 10 GeV to 3 TeV.

Figure 9 shows the 90% CL exclusions for the vector, axial vector, scalar and pseudoscalar mediator models. The expected 90% upper limit on  $\mu$  ( $\mu_{\text{up}}$ ), when assuming that the mediator only couples to fermions (fermionic), is shown by the blue color scale. The limits are calculated under the minimum width constraint [11, 12, 15, 68]. For the pseudoscalar interpretation, there is a region of masses between 150 and 280 GeV for which the decrease in cross section with larger mediator mass is balanced by an increase in acceptance for the signal, so that the expected signal contribution remains roughly constant. The expected value of  $\mu_{\text{up}}$  is larger than 1 for this region, resulting in an island at small DM. No exclusion is expected at the 90% CL therefore in this region. However, the observed value of  $\mu_{\text{up}}$  is smaller than 1 throughout this region at 90% CL so no such island appears in the observed limits.

The results are compared, for all four types of mediators, to constraints obtained from the observed cosmological relic density of DM as determined from measurements of the cosmic microwave background by the WMAP and Planck experiments [69, 70]. The expected DM abundance is estimated, separately for each model, using a thermal freeze-out mechanism implemented in MADDM1.0 [71], and compared to the observed cold DM density  $\Omega_c h^2 = 0.12$  [72] as described in Ref. [73]. It is assumed that the simplified model hypothesised provides the

only relevant beyond SM dynamics for DM interactions.

Figures 10(a) – 10(c) show the same exclusion contours, this time translated into the plane of  $m_{\text{DM}} - \sigma_{\text{SI/SD}}$ , where  $\sigma_{\text{SI/SD}}$  are the SI or SD (for vector and scalar or axial vector) DM-nucleon scattering cross sections. These representations allow for a more direct comparison with limits from the DD experiments, which typically set upper limits on these cross sections. The translations are obtained following the procedures outlines in Ref. [74] for the vector and axial vector mediators and Ref. [75] for the scalar mediator. It should be noted that the limits set from this analysis are only valid for the simplified model, and in particular assuming  $g_{\text{DM}} = g_{\text{SM}} = g_{\text{q}} = 1$ . For the scalar mediator model, it is assumed that only heavy quarks (top and bottom) contribute. Such a choice limits the sensitivity for DD experiments, but provide direct comparison between collider and DD experiments without an additional assumption on the light-quark couplings [75]. For vector and scalar mediator models, DD limits are stronger than those obtained in this analysis except in the scenario where the DM mass is less than around 6 GeV. For the axial vector mediator model, the limits obtained in this analysis dominate up to around  $m_{\text{DM}} = 300$  GeV.

For the vector and scalar models, the limits are compared with those from the LUX experiment [76]. The limits from the LUX experiment currently provide the strongest constraints on  $\sigma_{\text{SI}}$  for  $m_{\text{DM}} \gtrsim 4$  GeV [77]. For axial vector couplings, the limits are compared with DM–proton scattering limits from the PICO-2L [78], PICO-60 [79], IceCube [80] and Super-Kamiokande [81] experiments. For pseudoscalar interactions, direct detection bounds are strongly velocity suppressed. The most appropriate comparison is therefore to the most sensitive bounds from indirect detection from the Fermi LAT collaboration [82, 83]. These limits apply to the scenario in which dark matter is annihilated in the center of a galaxy, producing a  $\gamma$  ray signature.

In the vector mediator model, the constraints from this analysis are stronger than those from the DD experiments for  $m_{\text{DM}} < 4$  GeV as shown in Fig. 10(a). In the axial vector model, the limits from this analysis are stronger than the DD limits for much larger DM masses. Limits in the scalar mediator scenario are more sensitive than those from the DD experiments for  $m_{\text{DM}} < 6$  GeV as shown in Fig. 10(c).

An excess in  $\gamma$  ray emission, consistent with the annihilation of DM, at the galactic centre has been reported in several studies using data from Fermi LAT [84–86]. Further studies of this excess suggest that DM annihilation could be mediated by a light pseudoscalar [87, 88]. The production mechanism for these  $\gamma$  rays can be interpreted under DM annihilation to b quarks allowing for direct comparison with limits from this analysis [17, 89, 90]. Figure 10(d) shows the exclusion contours assuming pseudoscalar mediation in the plane of DM pair annihilation cross section versus  $m_{\text{DM}}$ . Again, it is assumed that only heavy quarks contribute in the production of the mediator while for the interpretation of the limits in the annihilation cross section, it is assumed that the mediator only decays to b quark pairs. As with all interpretations, the DM particle is assumed to be a Dirac fermion. The results shown from Fermi LAT have been scaled by a factor of 2 compared to Ref. [82] to translate the assumption of a Majorana DM fermion used in that analysis. The 68% CL preferred regions in this plane assuming the annihilation of DM pairs to light-quarks ( $q\bar{q}$ ),  $\tau^+\tau^-$  or  $b\bar{b}$ , using data from Fermi LAT, are shown as solid colour regions. For the simplified model, and assuming that  $g_{\text{DM}} = g_{\text{q}} = 1$ , all of these regions are excluded by this analysis. The limits from this analysis are stronger than those from Fermi LAT when the DM mass is below 100 GeV.

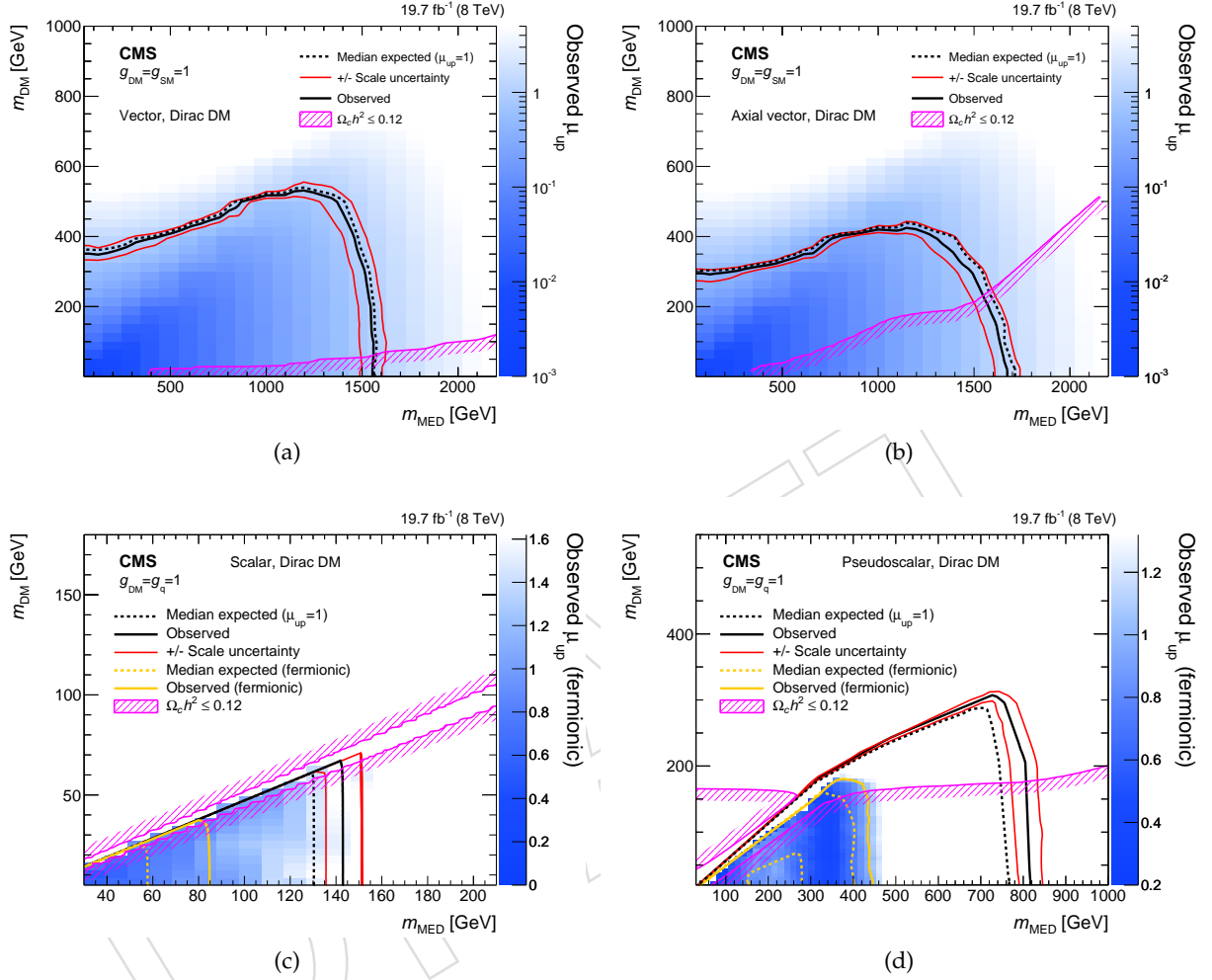


Figure 9: 90% CL exclusion contours in the  $m_{\text{MED}} - m_{\text{DM}}$  plane assuming (a) vector, (b) axial vector, (c) scalar, and (d) pseudoscalar mediators. The blue scale shows the expected 90% CL exclusion upper limit on the signal strength assuming the mediator only couples to fermions. For the scalar and pseudoscalar mediators, the exclusion contour assuming coupling only to fermions (fermionic) is explicitly shown by the orange line. The white region shows model points which were not tested when assuming coupling only to fermions and are not expected to be excluded by this analysis under this assumption. In all cases, the excluded region is to the bottom-left of the contours, except for the relic density which shows the regions for which  $\Omega_c h^2 = 0.12$ , as indicated by the shading. In all of the models, the mediator width is determined using the minimum width assumption.

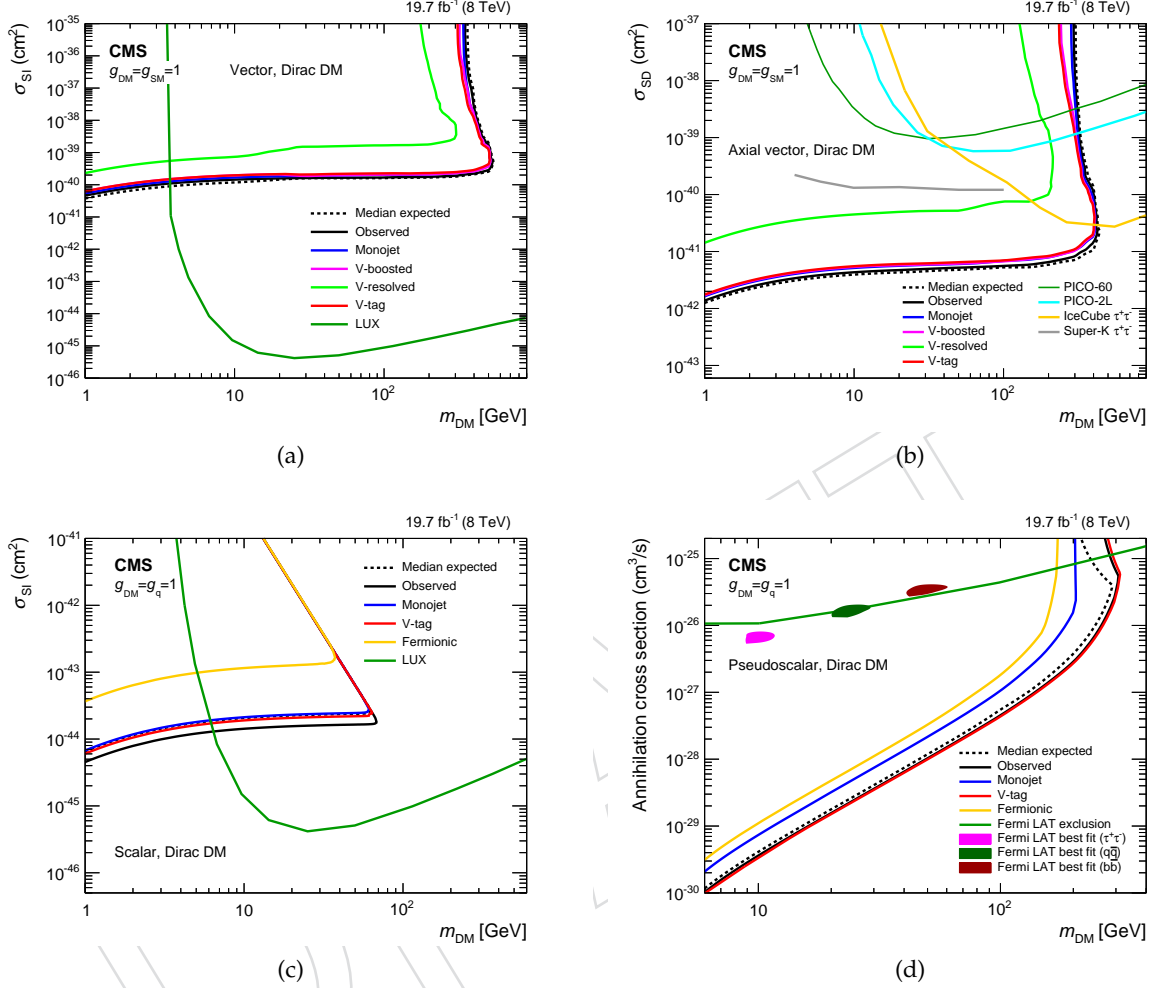


Figure 10: 90% CL exclusion contours in the  $m_{\text{DM}} - \sigma_{\text{SI}}$  or  $m_{\text{DM}} - \sigma_{\text{SD}}$  plane assuming (a) vector, (b) axial vector, (c) scalar mediators. 90% CL exclusion in DM annihilation cross section as a function of  $m_{\text{DM}}$  for a pseudoscalar mediator. For the scalar and pseudoscalar mediators, the orange line shows the exclusion contours assuming the mediator only couples to fermions (fermionic). The excluded region in all plots is to the top-left of the contours. In the vector and axial vector models, limits are shown independently for monojet, V-tagged and V-resolved categories. The partial combination of the V-tag categories is shown for which the V-boosted category provides the dominant contribution. In all of the mediator models, a minimum mediator width is assumed. For the pseudoscalar mediator, 68% CL preferred regions, obtained using data from Fermi LAT, for DM annihilation to light-quarks ( $q\bar{q}$ ), ( $\tau^+\tau^-$ ), and  $b\bar{b}$  are given by the solid green, pink and brown coloured regions, respectively.



## 7 Summary

A search has been presented for an excess of events with at least one energetic jet in association with a large missing transverse energy in a data sample of pp collisions at a centre-of-mass energy of 8 TeV. The data correspond to an integrated luminosity of  $19.7 \text{ fb}^{-1}$  collected with the CMS detector at the LHC. Sensitivity to a potential mono-V signature is achieved by the addition of two event categories which select hadronically decaying vector boson using novel jet substructure techniques. This search is the first at CMS to use jet substructure techniques to identify hadronically decaying vector bosons in both Lorentz-boosted and resolved scenarios. The sensitivity of the search has been increased compared to the previous CMS result by using the full shape of the  $E_T^{\text{miss}}$  distribution to discriminate signal from standard model backgrounds and through additional data control regions. No significant deviation is observed relative to the expectation from SM backgrounds in the  $E_T^{\text{miss}}$  distributions. The results of the search are interpreted under a set of simplified models, that describe the production of dark matter via vector, axial vector, scalar or pseudoscalar mediation and constraints on their parameter space are placed. The search excludes DM production via vector or axial vector mediation with mediator masses up to 1.5 TeV, within the simplified model assumptions. When compared to DD experiments, the limits from this analysis provide the strongest constraints at small DM masses. For scalar and pseudoscalar mediated DM production, this analysis excludes mediator masses up to 80 GeV and 400 GeV, respectively. The search is the first at CMS to be interpreted under these simplified models for DM production.

## Acknowledgments

We congratulate our colleagues in the CERN accelerator departments for the excellent performance of the LHC and thank the technical and administrative staffs at CERN and at other CMS institutes for their contributions to the success of the CMS effort. In addition, we gratefully acknowledge the computing centres and personnel of the Worldwide LHC Computing Grid for delivering so effectively the computing infrastructure essential to our analyses. Finally, we acknowledge the enduring support for the construction and operation of the LHC and the CMS detector provided by the following funding agencies: BMWFW and FWF (Austria); FNRS and FWO (Belgium); CNPq, CAPES, FAPERJ, and FAPESP (Brazil); MES (Bulgaria); CERN; CAS, MoST, and NSFC (China); COLCIENCIAS (Colombia); MSES and CSF (Croatia); RPF (Cyprus); MoER, ERC IUT and ERDF (Estonia); Academy of Finland, MEC, and HIP (Finland); CEA and CNRS/IN2P3 (France); BMBF, DFG, and HGF (Germany); GSRT (Greece); OTKA and NIH (Hungary); DAE and DST (India); IPM (Iran); SFI (Ireland); INFN (Italy); MSIP and NRF (Republic of Korea); LAS (Lithuania); MOE and UM (Malaysia); BUAP, CINVESTAV, CONACYT, LNS, SEP, and UASLP-FAI (Mexico); MBIE (New Zealand); PAEC (Pakistan); MSHE and NSC (Poland); FCT (Portugal); JINR (Dubna); MON, RosAtom, RAS and RFBR (Russia); MESTD (Serbia); SEIDI and CPAN (Spain); Swiss Funding Agencies (Switzerland); MST (Taipei); ThEP-Center, IPST, STAR and NSTDA (Thailand); TUBITAK and TAEK (Turkey); NASU and SFFR (Ukraine); STFC (United Kingdom); DOE and NSF (USA).

Individuals have received support from the Marie-Curie programme and the European Research Council and EPLANET (European Union); the Leventis Foundation; the A. P. Sloan Foundation; the Alexander von Humboldt Foundation; the Belgian Federal Science Policy Office; the Fonds pour la Formation à la Recherche dans l'Industrie et dans l'Agriculture (FRIA-Belgium); the Agentschap voor Innovatie door Wetenschap en Technologie (IWT-Belgium); the Ministry of Education, Youth and Sports (MEYS) of the Czech Republic; the Council of Science and Industrial Research, India; the HOMING PLUS programme of the Foundation for Polish Science, cofinanced from European Union, Regional Development Fund; the Mobility Plus programme of the Ministry of Science and Higher Education (Poland); the OPUS programme of the National Science Center (Poland); the Thalís and Aristeia programmes cofinanced by EU-ESF and the Greek NSRF; the National Priorities Research Program by Qatar National Research Fund; the Programa Clarín-COFUND del Principado de Asturias; the Rachadapisek Sompot Fund for Postdoctoral Fellowship, Chulalongkorn University (Thailand); the Chulalongkorn Academic into Its 2nd Century Project Advancement Project (Thailand); and the Welch Foundation, contract C-1845.

## References

- [1] CMS Collaboration, "Search for dark matter, extra dimensions, and unparticles in monojet events in proton proton collisions at  $\sqrt{s} = 8$  TeV", *Eur. Phys. J.* **C75** (2015) 235, doi:10.1140/epjc/s10052-015-3451-4, arXiv:1408.3583.
- [2] ATLAS Collaboration, "Search for new phenomena in final states with an energetic jet and large missing transverse momentum in pp collisions at  $\sqrt{s} = 8$  TeV with the ATLAS detector", *Eur. Phys. J.* **C75** (2015) 299, doi:10.1140/epjc/s10052-015-3517-3, 10.1140/epjc/s10052-015-3639-7, arXiv:1502.01518. [Erratum: *Eur. Phys. J.* **C 75** (2015) 408].

- [3] ATLAS Collaboration, “Search for dark matter candidates and large extra dimensions in events with a jet and missing transverse momentum with the ATLAS detector”, *JHEP* **04** (2013) 075, doi:10.1007/JHEP04(2013)075, arXiv:1210.4491.
- [4] ATLAS Collaboration, “Search for new phenomena with the monojet and missing transverse momentum signature using the ATLAS detector in  $\sqrt{s} = 7$  TeV proton-proton collisions”, *Phys. Lett. B* **705** (2011) 294–312, doi:10.1016/j.physletb.2011.10.006, arXiv:1106.5327.
- [5] CMS Collaboration, “Search for dark matter and large extra dimensions in monojet events in  $pp$  collisions at  $\sqrt{s} = 7$  TeV”, *JHEP* **09** (2012) 094, doi:10.1007/JHEP09(2012)094, arXiv:1206.5663.
- [6] CMS Collaboration, “Search for dark matter particles in proton-proton collisions at  $\sqrt{s} = 8$  TeV using the razor variables”, arXiv:1603.08914.
- [7] CMS Collaboration, “Search for physics beyond the standard model in final states with a lepton and missing transverse energy in proton-proton collisions at  $\sqrt{s} = 8$  TeV”, *Phys. Rev. D* **91** (2015) 092005, doi:10.1103/PhysRevD.91.092005, arXiv:1408.2745.
- [8] ATLAS Collaboration, “Search for dark matter in events with a Z boson and missing transverse momentum in  $pp$  collisions at  $\sqrt{s} = 8$  TeV with the ATLAS detector”, *Phys. Rev. D* **90** (2014) 012004, doi:10.1103/PhysRevD.90.012004, arXiv:1404.0051.
- [9] ATLAS Collaboration, “Search for dark matter in events with a hadronically decaying W or Z boson and missing transverse momentum in  $pp$  collisions at  $\sqrt{s} = 8$  TeV with the ATLAS detector”, *Phys. Rev. Lett.* **112** (2014) 041802, doi:10.1103/PhysRevLett.112.041802, arXiv:1309.4017.
- [10] ATLAS Collaboration, “Search for new particles in events with one lepton and missing transverse momentum in  $pp$  collisions at  $\sqrt{s} = 8$  TeV with the ATLAS detector”, *JHEP* **09** (2014) 037, doi:10.1007/JHEP09(2014)037, arXiv:1407.7494.
- [11] P. J. Fox, R. Harnik, J. Kopp, and Y. Tsai, “Missing energy signatures of dark matter at the LHC”, *Phys. Rev. D* **85** (2012) 056011, doi:10.1103/PhysRevD.85.056011, arXiv:1109.4398.
- [12] G., Busoni *et al.*, “On the validity of the effective field theory for dark matter searches at the LHC”, *Phys. Lett. B* **728C** (2014) 412., doi:10.1016/j.physletb.2013.11.069, arXiv:1307.2253.
- [13] O. Buchmueller, M. J. Dolan, and C. McCabe, “Beyond effective field theory for dark matter searches at the LHC”, *JHEP* **01** (2014) 025, doi:10.1007/JHEP01(2014)025, arXiv:1308.6799.
- [14] O. Buchmueller, M. J. Dolan, S. A. Malik, and C. McCabe, “Characterising dark matter searches at colliders and direct detection experiments: Vector mediators”, *JHEP* **01** (2015) 037, doi:10.1007/JHEP01(2015)037, arXiv:1407.8257.
- [15] D. Abercrombie *et al.*, “Dark matter benchmark models for early LHC Run-2 searches: Report of the ATLAS/CMS Dark Matter Forum”, (2015). arXiv:1507.00966.
- [16] CMS Collaboration, “The CMS experiment at the CERN LHC”, *JINST* **3** (2008) S08004.

- [17] P. Harris, V. V. Khoze, M. Spannowsky, and C. Williams, “Constraining Dark Sectors at Colliders: Beyond the Effective Theory Approach”, *Phys. Rev. D* **91** (2015), no. 5, 055009, doi:10.1103/PhysRevD.91.055009, arXiv:1411.0535.
- [18] U. Haisch, F. Kahlhoefer, and J. Unwin, “The impact of heavy-quark loops on LHC dark matter searches”, *JHEP* **07** (2013) 125, doi:10.1007/JHEP07(2013)125, arXiv:1208.4605.
- [19] L. Lopez-Honorez, T. Schwetz, and J. Zupan, “Higgs portal, fermionic dark matter, and a Standard Model like Higgs at 125 GeV”, *Phys. Lett. B* **716** (2012) 179–185, doi:10.1016/j.physletb.2012.07.017, arXiv:1203.2064.
- [20] V. V. Khoze, G. Ro, and M. Spannowsky, “Spectroscopy of scalar mediators to dark matter at the LHC and at 100 TeV”, *Phys. Rev. D* **92** (2015) 075006, doi:10.1103/PhysRevD.92.075006, arXiv:1505.03019.
- [21] T. Hambye and A. Strumia, “Dynamical generation of the weak and dark matter scale”, *Phys. Rev. D* **88** (2013) 055022, doi:10.1103/PhysRevD.88.055022, arXiv:1306.2329.
- [22] V. V. Khoze, C. McCabe, and G. Ro, “Higgs vacuum stability from the dark matter portal”, *JHEP* **08** (2014) 026, doi:10.1007/JHEP08(2014)026, arXiv:1403.4953.
- [23] V. V. Khoze and G. Ro, “Dark matter monopoles, vectors and photons”, *JHEP* **10** (2014) 61, doi:10.1007/JHEP10(2014)061, arXiv:1406.2291.
- [24] W. Altmannshofer et al., “Light dark matter, naturalness, and the radiative origin of the electroweak scale”, *JHEP* **01** (2015) 032, doi:10.1007/JHEP01(2015)032, arXiv:1408.3429.
- [25] C. D. Carone and R. Ramos, “Classical scale-invariance, the electroweak scale and vector dark matter”, *Phys. Rev. D* **88** (2013) 055020, doi:10.1103/PhysRevD.88.055020, arXiv:1307.8428.
- [26] M. Heikinheimo et al., “Physical Naturalness and Dynamical Breaking of Classical Scale Invariance”, *Mod. Phys. Lett. A* **29** (2014) 1450077, doi:10.1142/S0217732314500771, arXiv:1304.7006.
- [27] J. M. Campbell and R. K. Ellis, “MCFM for the Tevatron and the LHC”, *Nucl. Phys. Proc. Suppl.* **205-206** (2010) 10, doi:10.1016/j.nuclphysbps.2010.08.011, arXiv:1007.3492.
- [28] I. Anderson et al., “Constraining anomalous HVV interactions at proton and lepton colliders”, *Phys. Rev. D* **89** (2014) 035007, doi:10.1103/PhysRevD.89.035007, arXiv:1309.4819.
- [29] T. Sjöstrand, S. Mrenna, and P. Z. Skands, “PYTHIA 6.4 Physics and Manual”, *JHEP* **05** (2006) 026, doi:10.1088/1126-6708/2006/05/026, arXiv:hep-ph/0603175.
- [30] S. Agostinelli, J. Allison, K. Amako et al., “Geant4 — a simulation toolkit”, *Nucl. Phys. A* **506** (2003) 250, doi:http://dx.doi.org/10.1016/S0168-9002(03)01368-8.
- [31] NNPDF Collaboration, “Parton distributions for the LHC Run II”, *JHEP* **04** (2015) 040, doi:10.1007/JHEP04(2015)040, arXiv:1410.8849.

- [32] CMS Collaboration, “Particle-Flow Event Reconstruction in CMS and Performance for Jets, Taus, and MET”, CMS Physics Analysis Summary CMS-PAS-PFT-09-001, 2009.
- [33] M. Cacciari, G. P. Salam, and G. Soyez, “The Anti-kT jet clustering algorithm”, *JHEP* **04** (2008) 063, doi:10.1088/1126-6708/2008/04/063, arXiv:0802.1189.
- [34] CMS Collaboration, “A Cambridge-Aachen (C-A) based jet algorithm for boosted top-jet tagging”, CMS Physics Analysis Summary CMS-PAS-JME-09-001, 2009.
- [35] CMS Collaboration, “Determination of jet energy calibration and transverse momentum resolution in CMS”, *JINST* **6** (2011) 11002, doi:10.1088/1748-0221/6/11/P11002, arXiv:1107.4277.
- [36] M. Cacciari, G. P. Salam, and G. Soyez, “FastJet User Manual”, *Eur. Phys. J. C* **72** (2012) 1896, doi:10.1140/epjc/s10052-012-1896-2, arXiv:1111.6097.
- [37] CMS Collaboration, “Performance of Photon Reconstruction and Identification with the CMS Detector in Proton-Proton Collisions at  $\sqrt{s} = 8$  TeV”, *JINST* **10** (2015), no. 08, P08010, doi:10.1088/1748-0221/10/08/P08010, arXiv:1502.02702.
- [38] CMS Collaboration, “Performance of Electron Reconstruction and Selection with the CMS Detector in Proton-Proton Collisions at  $s = 8$  TeV”, *JINST* **10** (2015), no. 06, P06005, doi:10.1088/1748-0221/10/06/P06005, arXiv:1502.02701.
- [39] CMS Collaboration, “Reconstruction and identification of lepton decays to hadrons and at CMS”, *JINST* **11** (2016), no. 01, P01019, doi:10.1088/1748-0221/11/01/P01019, arXiv:1510.07488.
- [40] CMS Collaboration, “The performance of the CMS muon detector in proton-proton collisions at  $\sqrt{s} = 7$  TeV at the LHC”, *JINST* **8** (2013) P11002, doi:10.1088/1748-0221/8/11/P11002, arXiv:1306.6905.
- [41] CMS Collaboration, “The CMS Particle Flow Algorithm”, in *Proceedings, International Conference on Calorimetry for the High Energy Frontier (CHEF 2013)*, pp. 295–304. 2013. arXiv:1401.8155.
- [42] J. Alwall et al., “The automated computation of tree-level and next-to-leading order differential cross sections, and their matching to parton shower simulations”, *JHEP* **07** (2014) 079, doi:10.1007/JHEP07(2014)079, arXiv:1405.0301.
- [43] M. L. Mangano, M. Moretti, F. Piccinini, and M. Treccani, “Matching matrix elements and shower evolution for top-quark production in hadronic collisions”, *JHEP* **01** (2007) 013, doi:10.1088/1126-6708/2007/01/013, arXiv:hep-ph/0611129.
- [44] P. Nason, “A New method for combining NLO QCD with shower Monte Carlo algorithms”, *JHEP* **11** (2004) 040, doi:10.1088/1126-6708/2004/11/040, arXiv:hep-ph/0409146.
- [45] S. Frixione, P. Nason, and C. Oleari, “Matching NLO QCD computations with Parton Shower simulations: the POWHEG method”, *JHEP* **11** (2007) 070, doi:10.1088/1126-6708/2007/11/070, arXiv:0709.2092.
- [46] C. Oleari, “The POWHEG BOX”, *Nuc. Phys. B Proc. Sup.* **205** (2010) 36, doi:10.1016/j.nuclphysbps.2010.08.016, arXiv:1007.3893.



- [47] S. Alioli, P. Nason, C. Oleari, and E. Re, “A general framework for implementing NLO calculations in shower Monte Carlo programs: the POWHEG BOX”, *JHEP* **06** (2010) 043, doi:10.1007/JHEP06(2010)043, arXiv:1002.2581.
- [48] S. Alioli, P. Nason, C. Oleari, and E. Re, “NLO single-top production matched with shower in POWHEG:  $s$ - and  $t$ -channel contributions”, *JHEP* **09** (2009) 111, doi:10.1007/JHEP02(2010)011, 10.1088/1126-6708/2009/09/111, arXiv:0907.4076. [Erratum: *JHEP* **02**, (2010) 011].
- [49] J. Gao et al., “CT10 next-to-next-to-leading order global analysis of QCD”, *Phys. Rev. D* **89** (2014), no. 3, 033009, doi:10.1103/PhysRevD.89.033009, arXiv:1302.6246.
- [50] CMS Collaboration, “Performance of the CMS missing transverse momentum reconstruction in pp data at  $\sqrt{s} = 8$  TeV”, *JINST* **10** (2015) P02006, doi:10.1088/1748-0221/10/02/P02006, arXiv:1411.0511.
- [51] J. Thaler and K. Van Tilburg, “Identifying boosted objects with  $N$ -subjettiness”, *JHEP* **03** (2011) 015, doi:10.1007/JHEP03(2011)015, arXiv:1011.2268.
- [52] J. Thaler and K. Van Tilburg, “Maximizing boosted top identification by minimizing  $N$ -subjettiness”, *JHEP* **02** (2012) 093, doi:10.1007/JHEP02(2012)093, arXiv:1108.2701.
- [53] S. D. Ellis, C. K. Vermilion, and J. R. Walsh, “Recombination Algorithms and Jet Substructure: Pruning as a Tool for Heavy Particle Searches”, *Phys. Rev. D* **81** (2010) 094023, doi:10.1103/PhysRevD.81.094023, arXiv:0912.0033.
- [54] CMS Collaboration, “Identification techniques for highly boosted W bosons that decay into hadrons”, *JHEP* **12** (2014) 017, doi:10.1007/JHEP12(2014)017, arXiv:1410.4227.
- [55] CMS Collaboration, “V Tagging Observables and Correlations”, CMS Physics Analysis Summary CMS-PAS-JME-14-002, 2014.
- [56] J. Gallicchio and M. D. Schwartz, “Seeing in color: Jet superstructure”, *Phys. Rev. Lett.* **105** (2010) 022001, doi:10.1103/PhysRevLett.105.022001, arXiv:1001.5027.
- [57] E. Izaguirre, B. Shuve, and I. Yavin, “Improving identification of dijet resonances at hadron colliders”, *Phys. Rev. Lett.* **114** (2015) 041802, doi:10.1103/PhysRevLett.114.041802, arXiv:1407.7037.
- [58] CMS Collaboration, “Identification of b-quark jets with the CMS experiment”, *JINST* **8** (2013) P04013, doi:10.1088/1748-0221/8/04/P04013, arXiv:1211.4462.
- [59] J. H. Kuhn, A. Kulesza, S. Pozzorini, and M. Schulze, “Electroweak corrections to hadronic photon production at large transverse momenta”, *JHEP* **03** (2006) 059, doi:10.1088/1126-6708/2006/03/059, arXiv:hep-ph/0508253.
- [60] CMS Collaboration, “Performance of b tagging at  $\sqrt{s}=8$  TeV in multijet,  $t\bar{t}$  and boosted topology events”, CMS Physics Analysis Summary CMS-PAS-BTV-13-001, CERN, Geneva, 2013.
- [61] CMS Collaboration, “Measurement of the differential cross section for top quark pair production in pp collisions at  $\sqrt{s} = 8$  TeV”, *Eur. Phys. J.* **C75** (2015) 542, doi:10.1140/epjc/s10052-015-3709-x, arXiv:1505.04480.



- [62] CMS Collaboration, “Measurement of the  $pp \rightarrow ZZ$  production cross section and constraints on anomalous triple gauge couplings in four-lepton final states at  $\sqrt{s} = 8$  TeV”, *Phys. Lett. B* **740** (2015) 250, doi:10.1016/j.physletb.2014.11.059, arXiv:1406.0113.
- [63] CMS Collaboration, “Measurement of the  $W^+W^-$  cross section in pp collisions at  $\sqrt{s} = 8$  TeV and limits on anomalous gauge couplings”, arXiv:1507.03268. Submitted to *EPJC*.
- [64] “CMS Luminosity Based on Pixel Cluster Counting — Summer 2013 Update”, CMS Physics Analysis Summary CMS-PAS-LUM-13-001, CERN, 2013.
- [65] G. Cowan, K. Cranmer, E. Gross, and O. Vitells, “Asymptotic formulae for likelihood-based tests of new physics”, *Eur. Phys. J. C* **71** (2011) doi:10.1140/epjc/s10052-011-1554-0, 10.1140/epjc/s10052-013-2501-z, arXiv:1007.1727. [Erratum: *Eur. Phys. J. C* **73**, 2501 (2013)].
- [66] The ATLAS Collaboration, The CMS Collaboration, The LHC Higgs Combination Group Collaboration, “Procedure for the LHC Higgs boson search combination in Summer 2011”, Technical Report CMS-NOTE-2011-005. ATL-PHYS-PUB-2011-11, CERN, Geneva, Aug, 2011.
- [67] A. L. Read, “Presentation of search results: the CLs technique”, *J. Phys. G*: **28** (2002) 2693, doi:10.1088/0954-3899/28/10/313.
- [68] H. An, X. Ji, and L.-T. Wang, “Light dark matter and  $Z'$  dark force at colliders”, *JHEP* **07** (2012) 182, doi:10.1007/JHEP07(2012)182, arXiv:1202.2894.
- [69] WMAP Collaboration, “The Microwave Anisotropy Probe (MAP) mission”, *Astrophys. J.* **583** (2003) 1, doi:10.1086/345346, arXiv:astro-ph/0301158.
- [70] Planck Collaboration, “The scientific programme of Planck”, technical report, 2006. arXiv:astro-ph/0604069.
- [71] M. Backovic, K. Kong, and M. McCaskey, “MadDM v.1.0: Computation of dark matter relic abundance using MadGraph5”, *Phys. Dark Univ.* **5-6** (2014) 18, doi:10.1016/j.dark.2014.04.001, arXiv:1308.4955.
- [72] Planck Collaboration, “Planck 2013 results. XVI. Cosmological parameters”, *Astron. Astrophys.* **571** (2014) A16, doi:10.1051/0004-6361/201321591, arXiv:1303.5076.
- [73] T. du Pree, K. Hahn, P. Harris, and C. Roskas, “Cosmological constraints on dark matter models for collider searches”, (2016). arXiv:1603.08525.
- [74] S. A. Malik et al., “Interplay and characterization of dark matter searches at colliders and in direct detection experiments”, *Phys. Dark Univ.* **9-10** (2015) 51, doi:10.1016/j.dark.2015.03.003, arXiv:1409.4075.
- [75] P. Harris, V. V. Khoze, M. Spannowsky, and C. Williams, “Closing up on Dark Sectors at Colliders: from 14 to 100 TeV”, (2016). arXiv:1509.02904.
- [76] LUX Collaboration, “The large underground xenon (LUX) experiment”, *Nucl. Instrum. Meth. A* **704** (2013) 111, doi:10.1016/j.nima.2012.11.135, arXiv:1211.3788.

- [77] LUX Collaboration, “Improved limits on scattering of weakly interacting massive particles from reanalysis of 2013 LUX data”, *Phys. Rev. Lett.* **116** (2016) 161301, doi:10.1103/PhysRevLett.116.161301, arXiv:1512.03506.
- [78] PICO Collaboration, “Dark Matter Search Results from the PICO-2L C<sub>3</sub>F<sub>8</sub> Bubble Chamber”, *Phys. Rev. Lett.* **114** (2015), no. 23, 231302, doi:10.1103/PhysRevLett.114.231302, arXiv:1503.00008.
- [79] PICO Collaboration, “Dark matter search results from the PICO-60 CF<sub>3</sub>I bubble chamber”, *Phys. Rev. D* **93** (2016), no. 5, 052014, doi:10.1103/PhysRevD.93.052014, arXiv:1510.07754.
- [80] IceCube Collaboration, “Improved limits on dark matter annihilation in the Sun with the 79-string IceCube detector and implications for supersymmetry”, *JCAP* **1604** (2016), no. 04, 022, doi:10.1088/1475-7516/2016/04/022, arXiv:1601.00653.
- [81] Super-Kamiokande Collaboration, “Search for neutrinos from annihilation of captured low-mass dark matter particles in the Sun by Super-Kamiokande”, *Phys. Rev. Lett.* **114** (2015), no. 14, 141301, doi:10.1103/PhysRevLett.114.141301, arXiv:1503.04858.
- [82] Fermi-LAT Collaboration, “Constraining dark matter models from a combined analysis of milky way satellites with the Fermi large area telescope”, *Phys. Rev. Lett.* **107** (2011) 241302, doi:10.1103/PhysRevLett.107.241302, arXiv:1108.3546.
- [83] Fermi-LAT Collaboration, “Observations of milky way dwarf spheroidal galaxies with the Fermi-LAT detector and constraints on dark matter models”, *Astrophys. J.* **712** (2010) 147–158, doi:10.1088/0004-637X/712/1/147, arXiv:1001.4531.
- [84] C. Gordon and O. Macias, “Dark Matter and Pulsar Model Constraints from Galactic Center Fermi-LAT Gamma Ray Observations”, *Phys. Rev. D* **88** (2013), no. 8, 083521, doi:10.1103/PhysRevD.88.083521, 10.1103/PhysRevD.89.049901, arXiv:1306.5725. [Erratum: *Phys. Rev. D* **89**, no.4, 049901 (2014)].
- [85] K. N. Abazajian and M. Kaplinghat, “Detection of a Gamma-Ray Source in the Galactic Center Consistent with Extended Emission from Dark Matter Annihilation and Concentrated Astrophysical Emission”, *Phys. Rev. D* **86** (2012) 083511, doi:10.1103/PhysRevD.86.083511, 10.1103/PhysRevD.87.129902, arXiv:1207.6047. [Erratum: *Phys. Rev. D* **87**, 129902 (2013)].
- [86] D. Hooper and L. Goodenough, “Dark Matter Annihilation in The Galactic Center As Seen by the Fermi Gamma Ray Space Telescope”, *Phys. Lett. B* **697** (2011) 412–428, doi:10.1016/j.physletb.2011.02.029, arXiv:1010.2752.
- [87] P. Agrawal, B. Batell, P. J. Fox, and R. Harnik, “WIMPs at the Galactic Center”, *JCAP* **1505** (2015) 011, doi:10.1088/1475-7516/2015/05/011, arXiv:1411.2592.
- [88] F. Calore, I. Cholis, C. McCabe, and C. Weniger, “A tale of tails: dark matter interpretations of the Fermi GeV excess in light of background model systematics”, *Phys. Rev. D* **91** (2015) 063003, doi:10.1103/PhysRevD.91.063003, arXiv:1411.4647.
- [89] O. Buchmueller, S. A. Malik, C. McCabe, and B. Penning, “Constraining dark matter interactions with pseudoscalar and scalar mediators using collider searches for multijets plus missing transverse energy”, *Phys. Rev. Lett.* **115** (2015) 181802, doi:10.1103/PhysRevLett.115.181802, arXiv:1505.07826.

- 675 [90] M. R. Buckley, D. Feld, and D. Goncalves, “Scalar simplified models for dark matter”,  
676 *Phys. Rev. D* **91** (2015) 015017, doi:10.1103/PhysRevD.91.015017,  
677 arXiv:1410.6497.

DRAFT